



Cite this: DOI: 10.1039/d5ma00886g

Correlative characterization of stereocomplex formation in blends of aliphatic polyester P(PCL_m -*b*- PLA_n) multiblock-copolymers and PDLA

Armando Mandlule,^a Yue Liu,^a Susanne Schwanz,^a Yvonne Pieper,^a Heike Scharf,^a Kamila Iskhakova,^{bc} Andre L. C. Conceição,^b D. C. Florian Wieland,^d Berit Zeller-Plumhoff,^{de} Francesca M. Toma,^{af} and Axel T. Neffe^{id,*ag}

In phase-separating multiblock copolymers it is a challenge to quantify the relationship between molecular structure and functional properties, yet this quantification is crucial for processing and applications. Here, we describe the molecular structure and phase behavior-properties relationships for a modular system of poly(ϵ -caprolactone)-*b*-poly(L-lactide) multiblock copolymers with well-defined long/short block lengths and their blends with poly(D-lactide) (PDLA) of varying lengths. The formation of crystallite types and sizes as well as absolute and relative crystallinities of PCL, PLA homocrystallites (HC), and PLA stereocrystallites (SC) were studied by DSC and WAXS, and visualized by TEM, POM, and AFM. We reveal that SC formation occurs in blends containing a ratio between 1:1 and 1:4 ratio of PDLA and PLA. In systems with much longer PCL than PLA sequence length (113:18), SC formation is inhibited. Blend crystallinity was highest for a medium PDLA length. SC formation is preferred over HC formation, and SCs act as nucleation points for PCL crystallization. In our work the segment length had a trend to correlate with crystallite sizes. Tensile strength (from 0.5 to 8 MPa) and elongation at break (from 10% to >750% at room temperature) could be increased simultaneously by allowing SC formation, which in the studied blends correlated with low overall crystallinity. Our study shows strategic polymer synthesis and blending for the precise control of stereocomplex formation and fine-tuning in high-performance PLA-based materials. These findings support the knowledge-based choice of blend composition and segment length to tailor versatile materials with tunable mechanical and thermal properties.

Received 11th August 2025,
Accepted 11th November 2025

DOI: 10.1039/d5ma00886g

rsc.li/materials-advances

1. Introduction

Structure–property relationships in polymers are crucial for advancing sustainable material development. To reduce the environmental impact of waste plastics, hydrolytically degradable polymers such as polylactide (PLA), poly(ϵ -caprolactone) (PCL), polyglycolide (PGA), poly(*para*-dioxanone) (PDO), and

poly(trimethylene carbonate) (PTMC) have gained considerable attention.¹ These polymers are partially derived from renewable resources² and can potentially be chemically recovered.³ Functions such as the shape-memory effect^{4,5} can be implemented, which offers promise particularly in fields that prioritize sustainability and degradability.^{6–8} The material properties are inherently linked to their molecular structure, as the architecture and arrangement of polymer chains directly influence their ability to perform such tasks. The properties of the above-mentioned homopolymers often limit their applications. For example, isotactic and hence semicrystalline PLA is a brittle material with a relatively high Young's modulus of 3 to 3.5 GPa, but displays low elongation at break (only 2–10%) and poor impact strength.^{9,10}

PLA can be synthesized with both optically active L-lactide (LLA) and D-lactide (DLA) subunits. It can be either amorphous or semicrystalline, depending on their ratio and sequence structure. Additionally, PLA and its enantiomer PDLA can form a stereocomplex (sc-PLA). sc-PLA formation is driven by nucleation through $CH_3\cdots O=C$ hydrogen bonding and/or van

^a Helmholtz-Zentrum Hereon, Institute of Functional Materials for Sustainability, Kantstrasse 55, 14513 Teltow, Germany. E-mail: neffe@b-tu.de

^b Deutsches Elektronen-Synchrotron DESY, Notkestr. 85, 22607 Hamburg, Germany

^c Karlsruhe Institute of Technology, Institute for Chemical Technology and Polymer Chemistry, Engesserstr. 18/20, 76131 Karlsruhe, Germany

^d Helmholtz-Zentrum Hereon, Institute of Metallic Biomaterials, Max-Planck-Str. 1, 21502 Geesthacht, Germany

^e Data-driven Analysis and Design of Materials, Fakultät für Maschinenbau und Schiffstechnik, Universität Rostock, Albert-Einstein-Straße 2, 18059 Rostock, Germany

^f Faculty of Mechanical and Civil Engineering, Helmut Schmidt University, Hamburg 22043, Germany

^g Brandenburg University of Technology, Institute of Materials Chemistry, Universitätsplatz 1, 01968 Senftenberg, Germany

der Waals forces between L-lactide and D-lactide unit sequences.⁸ Stereocomplexes (SCs) between PDLA and PLLA exhibit significantly different properties compared to lactide homocrystallites (HC), due to their more ordered and tightly packed crystalline structure.¹¹ This includes a higher melting temperature (up to 220–230 °C compared to ~180 °C for homocrystallites),^{12,13} greater tensile strength, increased toughness, and slower hydrolytic degradation. Therefore, stereocomplexation of PLA offers one option to tailor the thermal and mechanical properties of PLA-based materials. This enhances the applicability of PLA in more demanding environments. To overcome the brittleness of PLA, several strategies have been employed, such as copolymerization,¹⁴ blending with softer (e.g. PCL) or rubber-like polymers, chemical modification, and the addition of additives.^{15,16}

Synthesis, structure and properties of homopolymers, copolymers, and diblock copolymers (DCs) of PLA have been extensively experimentally and theoretically studied.^{8,17} Properties are influenced by four levels of microstructure: the size of the crystals in the amorphous matrix, the interaction of neighboring chain segments, their symmetry, and defects. These levels are relatively well understood and can be controlled.¹⁸ Polylactide homocrystallites are formed in monodisperse oligomers with a minimum length of 11 units (~792 g mol⁻¹), whereas the minimum block length for stereocrystallization is 7 units (~504 g mol⁻¹).¹⁹ In copolymers, longer sequences seem necessary due to the reduced chain mobility. The smallest investigated crystallizable PLLA block had a number average molar mass (M_n) of 964 g mol⁻¹ (~13.4 repeating units) in PLLA–PCL diblock copolymers, while the PCL block required an M_n of 1133 g mol⁻¹ to crystallize with an amorphous PLLA part.²⁰ Moreover, the PCL block size required for crystallization increased to more than 2000 g mol⁻¹ when PLLA was crystalline.²⁰ This illustrates the interdependencies of polymer crystallite formation in systems containing multiple crystallizable components, particularly how crystallization of PLLA can inhibit PCL crystallization.

The structure–phase and structure–property relations in multiblock copolymers (MBCs) of PLA are not fully understood, compared to homopolymers, copolymers and DCs, though studies on other MBCs suggest similarities as well as peculiarities of MBCs compared to diblock copolymers.^{8,17,21} MBCs consist of sequences of two or more different polymer blocks, such as PLA and PCL, which are covalently bonded. MBCs offer a high degree of tunability by varying the block types, lengths and sequences. This would allow the design of materials with specific properties tailored to diverse applications. This versatility expands their potential use in fields such as medicine, electronics and packaging but also increases the complexity of the system. Understanding the structure–property relationships in MBCs is crucial for advancing and linking both fundamental polymer science and practical applications.^{22,23}

There are some selected examples of PLA-based MBCs and their blends reported, such as supramolecular PLLA–PCL MBCs, where PLA–PCL–PLA triblock copolymers are connected *via* ureido–pyrimidone units forming strong hydrogen-bonded

dimers and are mixed with PDLA (at a 1:1 ratio of PLLA to PDLA).²⁴ Here, it was found that the introduction of PCL blocks reduced the crystallite size of the stereocomplexes (as indicated by a lower melting temperature) and complicated homogeneous nucleation of stereocomplexes, but significantly improved the elongation at break and only slightly reduced the tensile strength of the blends. Additionally, self-condensation of PLLA–PCL diblock copolymers or individual PCL and PLLA blocks led to alternating or randomized PLLA–PCL MBCs, where stereocomplex formation is enabled in both types,^{25,26} as it is in blocky copolymers of PLLA and PCL.²⁷ Remarkably, the crystallization of MBCs influenced their interactions with proteins and cells, indicating potential applications in guiding cellular behavior, which is known to depend on factors like crystallization and mechanical properties.²⁸

During the development of reprogrammable and reversible shape–memory polymers, it was shown that PLLA sequence lengths in PLLA–PCL MBCs could be reduced to 15 units, and the added PDLA component could be reduced to six units while still permitting stereocomplex formation and reversible actuation.²³ This demonstrates the importance of MBC architectures in enabling precise control over material properties, as shorter block lengths can still achieve desired mechanical and thermal properties through stereocomplex formation. However, there is currently limited understanding on how varying block lengths and compositions within PLA–PCL-based MBCs affect their crystalline structures, SC formation,²⁹ and mechanical properties.^{30–32} Reported studies focused single handed either on their synthesis, mechanical properties, or miscibility and crystallization behavior of different phases. Hence, a comprehensive study is missing.

This study aims to fill this gap by systematically investigating four different combinations of P(PCL-*b*-PLLA)_x MBCs: (i) short PCL/short PLLA (s/s), (ii) short PCL/long PLLA (s/l), (iii) long PCL/short PLLA (l/s), and (iv) long PCL/long PLLA (l/l). This selection enables a detailed examination of how block lengths influence the formation of different crystalline phases, including SCs and homocrystallites (HCs) (Fig. 1). Moreover, the study also explores the role of poly(D-lactide) (PDLA) with varying chain lengths (15, 29, or 56 units) in SC formation, as the mobility of individual chains plays a critical role in determining the crystalline phase and overall crystallinity.¹⁹

To comprehensively understand the structure–property relationships in these MBCs, a multimodal and correlative characterization approach is employed. This approach integrates multiple analytical techniques, including differential scanning calorimetry (DSC), wide-angle X-ray scattering (WAXS), polarized optical microscopy (POM), atomic force microscopy (AFM), and transmission electron microscopy (TEM) to correlate the molecular structure and phase behavior with the mechanical properties. By combining these methods, we can obtain a comprehensive view of molecular architecture, formation of crystalline phases in relation to block lengths and how these microstructural features influence the macroscopic properties of these MBCs. Through this systematic investigation, we aim to establish detailed molecular structure/phase structure/



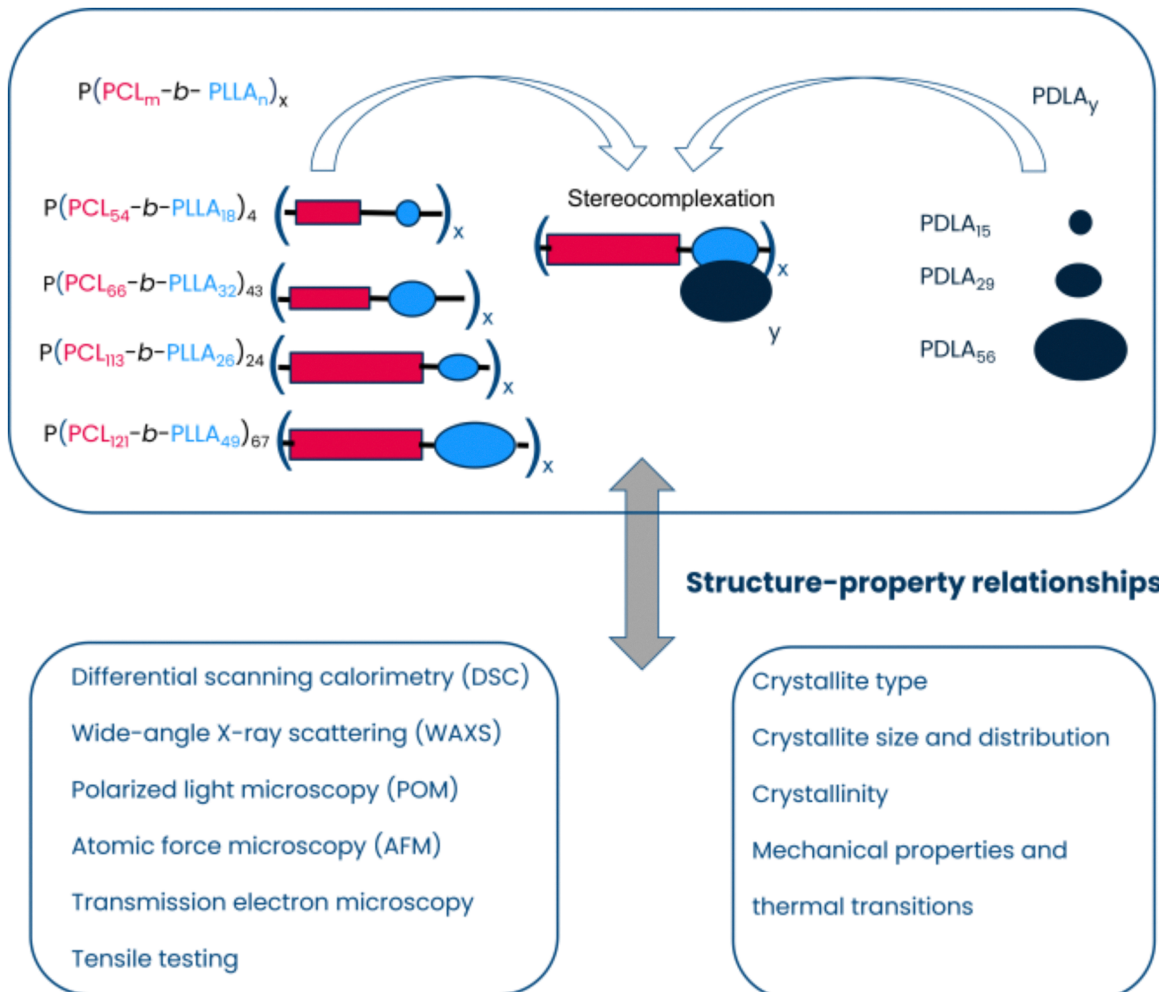


Fig. 1 Synthesized multiblock copolymers ($P(PCL_m-b-PLLA_n)_x$) consisting of different block lengths PCL (red) and PLLA (blue) with specific repeating units are blended with PDLA (black) of different chain lengths and the microstructure, sc-PLA formation and properties of the blends are investigated in terms of crystallite types, size, distribution and the phase structure relation to macroscopic mechanical properties.

property relationships in PLA-PCL MBCs, contributing valuable insights into phase formation and the ability to tailor polymer properties for specific applications. This knowledge could have significant implications for the development of new materials in biomedicine, packaging, and other technical fields.

2. Materials & methods

2.1. Materials

The synthesis involved the use of the following chemicals as received: chloroform (99.9%), toluene (99.5%), methanol (99%), tetrahydrofuran (THF) (99.9%) and dichloromethane (DCM) (99.9%) were purchased from Carl Roth, Karlsruhe, Germany. Dimethylaminopyridine (DMAP) (99%), *p*-toluenesulfonic acid monohydrate (pTSA) (98.5%), deuterated chloroform (99.8%) and *N,N'*-diisopropylcarbodiimide (DIPC) (98%) were purchased from Sigma-Aldrich, Missouri, USA. Anhydrous 1-hexanol (99%, Acros Organics, Geel, Belgium), tin(II)-2-hexanoate (96%, Alfa Aesar, Massachusetts, USA), anhydrous benzyl alcohol (BnOH)

(98%, Acros Organics, Geel, Belgium), 10% palladium on activated carbon (Alfa Aesar, Massachusetts, USA), *L,L*-dilactide (99.5%, Corbion, Amsterdam, Netherlands), and *D,D*-dilactide (99.5%, Corbion, Amsterdam, Netherlands), were stored over molecular sieves. ϵ -Caprolactone (99%, Acros Organics, Geel, Belgium) was distilled before use. Dimethylaminopyridine 4-toluenesulfonate (DMAP·pTSA) was prepared as previously described.^{25,33}

2.2. Synthesis

The synthesis of PLLA-PCL multiblock copolymers ($P(PCL_m-b-PLLA_n)_x$ MBCs) involves four distinct reaction steps and has been reported by Izraylit *et al.* before.²⁶ The full reaction scheme (ROP of PCL, ROP of PLLA, hydrogenation, polycondensation) is shown in the SI (Scheme S1). Firstly, the PCL block was synthesized through ring-opening polymerization (ROP) of CL using benzyl alcohol (BnOH) as initiator and tin(II)-2-hexanoate ($SnOct_2$) as catalyst. Prior to the polymerization, all glassware was dried overnight in an oven at 200 °C and further heated with a heating gun which was set to 600 °C under



vacuum for fifteen minutes, then purged with argon three times. Subsequently, ϵ -caprolactone was vacuum distilled before being combined with anhydrous BnOH (1 : x) and SnOct₂ (1 : 2000) in a round bottom flask. The amount of BnOH, which acts as an initiator, was calculated depending on which molar mass was targeted. The polymerization process was conducted under an argon atmosphere for 2.5 h at 120 °C. The resulting polymer was cooled to room temperature, dissolved in chloroform (300 mL), and precipitated in cold methanol (1 L) under stirring. After 5 h of refrigeration, the precipitate was filtered and dried in a vacuum oven at 110 °C for 36 h to remove residual components. Finally, a sample was subjected to ¹H-NMR and GPC analyses to verify molar mass and conversion rate.

Secondly, the benzyl-protected poly[$(\epsilon$ -caprolactone)-*block*-(L-lactide)] was synthesized *via* ROP of L,L-dilactide with the previously synthesized PCL as the macroinitiator. For calculating the amount of initiator (Bn-PCL), the molar mass of Bn-PCL determined by ¹H-NMR was used. Initially, Bn-PCL was transferred to a reaction flask containing L,L-dilactide under argon flux. The reaction vessel was then heated to 140 °C using an oil bath, and Sn(Oct)₂ (1 : 500) was added *via* a syringe. After 4 hours, the reaction mixture was cooled, dissolved in 300 mL of chloroform, and precipitated into 1 L methanol, yielding a white precipitate. This precipitate was filtered through a glass filter with an average pore size of 10–16 μ m and subsequently dried under vacuum.

Next, the benzyl protection group was removed from benzyl-protected poly[$(\epsilon$ -caprolactone)-*block*-(L-lactide)] *via* hydrogenation. A solution containing the block copolymer (max. 30 g) dissolved in 150 mL of THF was introduced into a Büchi ecoclave reactor. Subsequently, 300 mg of Pd/C catalyst was added, and the reaction was allowed to proceed for 28–36 h at 50 °C under a hydrogen atmosphere (5 bar). After completion, which was indicated by a decrease in pressure, the reaction mixture was precipitated into cold methanol, yielding a white precipitate that was filtered through a glass filter with an average pore size of 10–16 μ m and then dried under vacuum.

Lastly, the final multiblock copolymer P(PCL_m-*b*-PLLA_n)_x was synthesized through a block extension *via* polycondensation reaction of the PCL-PLLA diblock copolymers. The synthesis principle and the synthesis of DMAP-pTSA or 4-dimethylaminopyridinium 4-toluenesulfonate (DPTS) has been described previously.^{25,33} Initially, the multiblock copolymer was dissolved in 100 mL of toluene and dried using a rotary evaporator to remove water traces. The resulting multiblock copolymer was transferred to a reaction flask under argon and dissolved in DCM. Subsequently, 0.2 equivalents of DMAP, 0.2 equivalents of DMAP-pTSA, and 4 equivalents of DIPC were added. The M_n of the unprotected diblock determined by GPC was used for the calculation of DMAP, DMAP-pTSA and DIPC. The reaction was allowed to proceed for 3 days at room temperature under stirring. The end of the reaction was indicated by the crystallization of the polymer in the reaction vessel, if the viscosity became too high during the reaction and the magnetic stirrer stopped rotating, additional solvent was added. The reaction mixture was then diluted with 300 mL of DCM and precipitated

into methanol (1 L), resulting in a white solid precipitate. This precipitate was filtered and dried under a vacuum.

Poly(D-lactide) was synthesized by a ring opening polymerization of D,D-dilactide by using 1-hexanol as initiator and tin(II)-2-hexanoate (SnOct₂) as catalyst. The reaction was conducted at 140 °C for 60 minutes under an argon atmosphere and the resulting polymer was dissolved in chloroform. Afterwards, the product was precipitated in cold methanol and washed 3 times with methanol. Subsequently the polymer was dried in a vacuum oven until a constant mass was achieved.

Films were fabricated through blending poly[$(\epsilon$ -caprolactone)-*block*-(L-lactide)] (P(PCL_m-*b*-PLLA_n)_x) MBCs with poly(D-lactide) (PDLA) at predetermined weight percentage ratios. The respective amounts of Multiblock and PDLA were carefully weighed and dissolved in chloroform with stirring over a 24-hour period. Subsequently, the solutions were poured into a PTFE Petri dish, covered with aluminum foil, and the solvent was allowed to evaporate under ambient conditions for another 24 hours. Finally, the films were subjected to drying in a vacuum drying oven under vacuum (0.01 mbar) at 25 °C for 3 days to remove residual solvent.

2.3. Characterization

2.3.1. Nuclear magnetic resonance spectroscopy (¹H-NMR).

¹H-NMR spectra were acquired at room temperature using a DRX Avance 500 MHz or 700 MHz spectrometer (Bruker, Rheinstetten, Germany), with deuterated chloroform (CDCl₃) as the solvent and conducting 128 scans. Prior to analysis, the samples were dissolved at room temperature using a concentration of 15 μ g mL⁻¹, and the solution was filtered with a cotton filter before the analysis. Signal positions (ppm) and integrals from respective groups were considered during spectrum evaluation. The spectra were individually referenced to the residual solvent protons of chloroform at 7.26 ppm. To assess molar mass based on the obtained ¹H-NMR data, an estimated error of 12% was accounted for, considering factors such as saturation effects, intensity losses from isotropic sidebands, sample non-uniformity in the magnetic field, and line shape contributing to peak overlapping.³⁴ The molecular structures of PCL, PCL-*b*-PLLA diblock copolymers and P(PCL_m-*b*-PLLA_n)_x multiblock copolymers were assigned according to the work of Izrailit *et al.*²⁶ The degree of polymerization (DP) for PCL was calculated using the following equations:

$$DP_n(PCL) = \frac{5 \times I_{CH_2}}{2 \times I_{Bn}} + 1 \quad (1)$$

with the integral I_{Bn} at ~7.3–7.4 ppm, while for the I_{CH₂} the –CH₂–O group at ~4.1 ppm was used. The +1 is due to the terminal group that is not represented in the integral at 4.1 ppm. The number-average molecular weight (M_n) was then calculated as:

$$M_n(PCL) = DP_n \times M_0(PCL) + M_{\text{end groups}} \quad (2)$$

where M₀ (PCL) is the molar mass of one PCL repeat unit (114.14 g mol⁻¹), and M_{end groups} corresponds to the total molar mass of the terminal groups (*e.g.*, benzyl and hydroxyl =



108.14 g mol⁻¹). The degree of polymerization of both blocks was determined from the integral ratios of the end-group protons to the methine protons of the PLA block ($\delta \sim 5.2$ ppm) and the methylene CH₂-O protons of the PCL block ($\delta = 4.1$ ppm):

$$DP_n(\text{PLA}) = \frac{3 \times I_{\text{CH}}}{2 \times I_{\text{Bn}}} \quad (3)$$

and the number-average molar mass (M_n) was then calculated as:

$$M_n(\text{Di-block}) = (DP_n(\text{PCL}) \times M_0(\text{PCL})) + (DP_n(\text{PLA}) \times M_0(\text{PLA})) + M_{\text{end groups}} \quad (4)$$

with $M_0(\text{PLA}) = 72.07$ g mol⁻¹.

2.3.2. Gel permeation chromatography (GPC). The molar mass and its distribution of the polymers were determined *via* gel permeation chromatography (GPC) using a Tosoh EcoSEC HLC-8320 Gel Permeation Chromatograph equipped with a refractive index detector (Tosoh Bioscience, Stuttgart, Germany). This setup was complemented with a PSS Universal Data Center (PSS, Mainz, Germany), a viscometer ETA2010 (PSS, Mainz, Germany), an EcoSEC UV detector 8320 (Tosoh Bioscience), and a light scattering detector SLD7100 (PSS, Mainz, Germany). Two HT-GPC columns of type PSS SDV analytical linear M 5 μm (PSS, Mainz, Germany) were connected in series for analysis.

During measurements, chloroform (CDCl₃) stabilized with ethanol (0.6–1%) was utilized as the eluent, maintained at 35 °C with a flow rate of 1.0 mL min⁻¹. Additionally, 0.05 weight content toluene served as an internal standard to ascertain the hydrodynamic volume relative to elution volume. Molar mass and dispersity calculations were executed using WINGPC 6.2 (PSS) SEC software (Polymer Standard Service, Mainz, Germany). An error margin of 10% of the measured value was considered, accounting for variations in the measurement of polystyrene calibration standards.

2.3.3. Differential scanning calorimetry (DSC). DSC measurements were performed on a Netzsch DSC 204 Phoenix (Netzsch, Selb, Germany) to determine the crystallization – (T_c), melting – (T_m) and the glass transition-temperatures (T_g) and their respective enthalpies of the polymers and their blends. For the peak areas an error of 1 °C and for the measured enthalpies an error of 10% were considered in the evaluation. Measurements have been performed on 5–5.5 mg polymer sample under a nitrogen atmosphere by using heating and cooling rates of 10 K min⁻¹ in the range of –100 to 230 °C. For the calculated relative crystallite content of the polymer blends the first heating run was used and, in a further step, compared to the calculated crystallinities obtained by WAXS measurements. From the determined melting and crystallization enthalpy values of the measurements the relative crystallite content (χ_c) of all components have been calculated, according to eqn (5):

$$\chi_c = \frac{\Delta H_m}{\text{wt}_x \times \Delta H_m^0} \times 100\% \quad (5)$$

and the absolute crystallite content was calculated according to

eqn (6):

$$\phi_c = \frac{\Delta H_m}{\Delta H_m^0} \times 100\% \quad (6)$$

where ΔH_m is the experimental melting enthalpy of a fraction, determined as the area under the melting peak and wt_x is the mass fraction of PDLA, PLLA, PCL or sc-PLA in the respective mixture. For the calculations of sc-PLA the lower amount of either PDLA or PLLA content, which was present in P(PCL_m-b-PLLA_n)_x:PDLA_y was used and multiplied by two. This represents the percentage of a PLLA:PDLA 1:1 mixture. ΔH_m^0 is the specific melting enthalpy of 100% crystalline polymer, which is 135 J g⁻¹ for PCL,³⁵ 142 J g⁻¹ for PLA stereocomplex³⁶ and 93 J g⁻¹ for a 100% crystalline PLLA or PDLA homocrystallites.³⁷ For samples in which cold crystallization occurred during the first heating run, the relative crystallinity was calculated according to eqn (7):

$$\chi_c = \frac{(\Delta H_m - \Delta H_{cc})}{\text{wt}_x \times \Delta H_m^0} \times 100\% \quad (7)$$

where ΔH_m is the enthalpy of melting, ΔH_{cc} is the cold crystallization enthalpy, ΔH_m is the melting enthalpy for a 100% crystalline PLLA, sc-PLA, PCL or PDLA and wt_x is the mass fraction of PDLA, PLLA, PCL or sc-PLA in the respective mixture.

2.3.4. X-ray crystallographic analysis (WAXS & synchrotron). Lab WAXS measurements were performed at room temperature with a D8 Discover diffractometer using a 2D-detector from Bruker AXS (Karlsruhe, Germany). The samples of dimensions 2 × 0.5 cm and width 50 μm were fixed at both ends during characterization. Peak position was determined with an error of $\Delta\theta = 0.1^\circ$, originating from variations in sample thickness and position in the sample holder. The X-ray generator producing copper K- α radiation with a wavelength of 0.154 nm was operated at a voltage of 40 kV and a current of 40 mA. A graphite monochromator and a pinhole collimator with an opening of 0.8 mm defined the optical and geometrical properties of the beam.

The synchrotron WAXS measurements were performed at the beamline P62 at the Petra III storage ring, Deutsche Electron Synchrotron Facility (DESY), Hamburg at the SAXS-MAT beamline P62,³⁸ with a beam size of 700 × 400 μm ($H \times V$), and a wavelength of 0.103 nm. As a calibrant for WAXS silicon powder (Si) was used. To avoid local differences in composition, the sample was measured at three different locations. Analysis of peak positions and full width at half-maximum (FWHM) values provided information regarding crystallite size and degree of crystallinity (relative content). The crystal sizes (L) were calculated according to the Scherrer equation:³⁹

$$L = \frac{K \times \lambda}{\Delta \text{FWH} \times \cos 2\theta} \times 100\% \quad (8)$$

where L is the expansion of the crystal perpendicular to the planes of the reflection, K (0.9) is the Scherrer form factor, λ is the wavelength of the X-rays, ΔFWH is the full half-width of the reflex after correction of the instrument-related broadening

measured in radians and 2θ is the Bragg angle. The WAXS profiles in the 2θ range of $10\text{--}30^\circ$ were processed using the P62 reduction tool, which included steps for converting 2D to 1D data, azimuthal integration, and correction for instrumental broadening. The processed data were initially fitted using Voigt profiles, as implemented in the P62 tool, to account for the contributions of instrumental broadening (Gaussian component) and crystallite size or strain effects (Lorentzian component).

Subsequently, the graphs were manually analyzed, and the areas under the peaks corresponding to the respective phases (amorphous, stereocomplex crystals, PCL crystals, and homocrystals) were evaluated. The area under the curve obtained from the Voigt fit (e.g., 34.38) closely matched that of a Gaussian fit (e.g., 34.04). For simplicity and to facilitate phase quantification, Gaussian curves were ultimately adopted. This decision was based on the negligible difference in the calculated areas between the two fitting methods and the ease of interpreting Gaussian functions for phase analysis. The subtraction of the amorphous phase from the overall profiles is illustrated in Fig. S3 in the SI. The relative degree of crystallinity (X_c) was calculated according to the following relation:

$$X_c = \frac{I_c}{I_c + I_a} \times 100\% \quad (9)$$

where I_c represent the integrated intensities under the crystalline diffraction peaks and I_a the intensities of the amorphous halo.

2.3.5. Transmission electron microscopy (TEM). In order to further explore the changes in the morphology of the different compositions of the polymer, TEM measurements are carried out. A FEI Talos F200X transmission electron microscope (Thermo Fisher Scientific, Massachusetts, USA) equipped with a Ceta 16 M camera and a Single-tilt holder was used and operated at 200 kV, to obtain the high-resolution transmission electron microscope (HRTEM) images of the samples. All samples for morphology observation were taken by immersing a carbon copper Lacey grid in the respective polymer solution. As the solvent evaporated, a free-standing polymer film formed, spread over the holes of the Lacey-C film. The films were then stained with ruthenium tetroxide (0.5% in H_2O) vapor for 20 min.

2.3.6. Atomic force microscopy (AFM). The polymer films and prepared TEM grids were investigated by an AFM MFP-3D (Asylum Research, Santa Barbara, CA, USA). A Diamond-Like-Carbon Coated Force Modulation AFM Probe (Multi75DLC, BudgetSensors, Bulgaria) with a nominal spring constant of 3 N m^{-1} and a nominal tip radius of 15 nm was used. Before each measurement, the spring constant and inverse optical lever sensitivity of the probe were calibrated using GetReal™ automated probe calibration provided by Asylum Research. AFM images were acquired by operating the AFM in AM-FM mode at room temperature. This technique, developed by Asylum Research, is used to measure the viscoelasticity of materials. The first resonance is utilized in amplitude modulation (AM) mode for tapping mode topography and phase images, while the higher resonance mode is employed in frequency modulation (FM) mode to determine the elastic modulus.⁴⁰ A digital resolution of 256 lines \times 256 points for

$1 \mu\text{m} \times 1 \mu\text{m}$ or 512 lines \times 512 points for $5 \mu\text{m} \times 5 \mu\text{m}$ and a scanning rate of 1.00 Hz was used. Both height and phase images were acquired simultaneously. Silicon cantilever tips with resonance frequency of approximately 300 kHz and a spring constant of about 40 N m^{-1} were applied in all experiments.

2.3.7. Polarized optical microscopy (POM) & annealing.

Polarized optical microscopy (POM) observations of the samples were performed with a ZEISS Axio Imager 2 Pol microscope equipped with a hot stage (Linkam LTS350). The films were melted on a Linkam LTS350 hot stage, and, afterwards, annealed according to the melting and crystallization temperatures determined in DSC measurements. The Linkam LTS350 hot stage was equipped with a liquid-nitrogen cooling system (LNP) with a maximum cooling rate of $30 \text{ }^\circ\text{C min}^{-1}$. The morphology changes were recorded at according to the melting temperatures of the individual constituents.

2.3.8. Mechanical testing. The produced films were cut into dog-bone-shaped specimens for tensile testing. The samples' thicknesses, widths, and valid lengths were approximately 0.45, 3.0, and 15.0 mm. The test results were the average of three tests. All mechanical tests were carried out using a thermomechanical tensile tester Zwick Z1.0 (Ulm, Germany) with a temperature controller. All studies employed a clamping distance of 10 mm and were performed at room temperature with a constant deformation rate of 10 mm min^{-1} until breaking occurred.

3. Results & discussion

3.1. Synthesis and characterization of $\text{P}(\text{PCL}_m\text{-}b\text{-PLLA}_n)_x$ MBCs and PDLA

Four different $\text{P}(\text{PCL}_m\text{-}b\text{-PLLA}_n)_x$ multiblock copolymers (I/I, I/s, s/I, s/s) have been synthesized (Table 1), varying in both the relative content as well as the molar mass of each block in the multiblock copolymer (synthesis see SI Scheme S1). The synthesis route of $\text{P}(\text{PCL}_m\text{-}b\text{-PLLA}_n)_x$ as well as of PDLA follows published procedures, with details of structure determination given in the SI (including Fig. S1 and S2). The MBC synthesis *via* self-polycondensation has the advantage that no chain extenders need to be used, which may bring in a further glassy or crystalline phase or whose remnants might be harmful limiting potential biomedical applications.²⁵ Because the molar ratio between the carboxy and hydroxy groups continues to remain at 1:1, stoichiometry is not an issue in the polycondensation to reach high molar mass. However, high conversion was only accessible by continued stirring, which at times required addition of small amounts of solvent during this reaction.

The molar mass of the di-blocks was determined by $^1\text{H-NMR}$ using the benzyl end group as a reference. To determine the molar mass of PCL by $^1\text{H-NMR}$ (see SI Fig. S1 for an assigned example spectra), the aromatic protons of the benzyl end group (integral A; $\delta = 7.3\text{--}7.4 \text{ ppm}$) (use of the signal of benzylic protons at 5.115 ppm gave similar results) were used as an internal reference and compared to the $\text{CH}_2\text{-O}$ methylene protons (integral F; $\delta = 4.1 \text{ ppm}$) within the polymer backbone. The integration ratio of the aromatic and benzylic protons of



Table 1 Overview of the molar masses and dispersities of the synthesized di- and multiblock copolymers and PDLA's determined by ^1H -NMR and/or GPC

Sample	M_n ^1H -NMR (g mol $^{-1}$)	M_n GPC b (g mol $^{-1}$)	M_w GPC (g mol $^{-1}$)	D
P(PCL ₅₄ - <i>b</i> -PLLA ₁₈) ₄ (s/s)	7560 ^a	35 000	51 600	1.4
P(PCL ₆₆ - <i>b</i> -PLLA ₃₂) ₄₃ (s/l)	9940 ^a	420 000	710 000	1.6
P(PCL ₁₁₃ - <i>b</i> -PLLA ₂₆) ₂₄ (l/s)	14 860 ^a	370 000	600 000	1.6
P(PCL ₁₂₁ - <i>b</i> -PLLA ₄₉) ₂₆ (l/l)	17 430 ^a	450 000	900 000	1.6
PDLA ₁₅	1200	2800	3100	1.1
PDLA ₂₉	2200	3300	3600	1.1
PDLA ₅₆	4100	3500	4400	1.2

^a Molar mass of Bn-PCL-PLLA di-block determined by ^1H -NMR, which was used to synthesize the MBC. ^b Molar mass of P(PCL-*b*-PLLA)_x multiblock determined by GPC, which is based on the di-block.

initiator and the $\text{CH}_2\text{-O}$ methylene protons at the end of the chain (3.6 ppm) was 5:2:2, confirming the formation of the PCL oligomer with the corresponding end groups. Full details of the calculation is given in the Experimental section.

In the second step, DIBCs were synthesized using Bn-PCL as the macroinitiator and $\text{Sn}(\text{Oct})_2$ as the catalyst at 130 °C. The degree of polymerization (DP) of both LA and PCL in the PCL-*b*-PLLA diblock copolymers was calculated from the integration ratio of peaks of the Bn end group (integral A) to integral G/G' and F, as shown in Fig. S1. The resulting copolymer composition closely matched the feed molar ratio of LA to PCL.

In the third step, the benzyl end group of the di-block copolymer was removed by hydrogenation to enable subsequent chain extension in both directions during the fourth reaction step. The successful cleavage of the end group was verified by ^1H -NMR, and the corresponding decrease in molecular weight was consistent with the loss of the benzyl moiety. The following polycondensation reaction was carried out for 48 h at room temperature in the presence of *N,N'*-diisopropylcarbodiimide (DIC), 4-(dimethylamino)pyridine (DMAP), and 4-dimethylaminopyridine-4-toluenesulfonate (DMAP-TsOH). The generated water was trapped as urea, driving the reaction forward. During polycondensation, the viscosity of the mixture increased substantially, requiring small additions of solvent to maintain efficient mixing. As a result of the step-growth chain extension, the molecular weight increased considerably up to $M_n \approx 4.5 \times 10^5$ g mol $^{-1}$.

Due to this increase in molar mass, the ^1H signals of the end groups became hence negligible compared to the polymer backbone so that integration gave too large errors to allow accurate determination of M_n by ^1H NMR (in our case: deviation from the GPC data by up to 80%), so the molar mass and molar mass distribution of the MBCs was determined by universally calibrated GPC, assuming that the block ratio remained constant during polycondensation. The molar masses obtained by NMR for the diblock precursors were used as the reference.

In the following, multiblock copolymers P(PCL_{*m*}-*b*-PLLA_{*n*})_{*x*} are stated with the respective number of repeating units of CL(*m*), L-LA(*n*) and the diblock (*x*). Blends are designated as P(PCL_{*m*}-*b*-PLLA_{*n*})_{*x*}:PDLA_{*y*}ZZ, with *y* being the number of repeating units in the PDLA, and ZZ the weight% content of the multiblock copolymer in the blend.

3.2. Present crystallite phases & conditions for SC formation

The distinction between stereocomplex (SC) and homocrystallite (HC) formation was determined based on combined structural and thermal analysis. Specifically, SC formation was identified by characteristic diffraction peaks and melting transitions distinct from those of HC crystals as explained below. The first question addressed was whether PCL crystallites, PLA HCs or PLA SCs form in the different MBCs and their blends with PDLA of different length and in different blend compositions, and if yes, to which extent. WAXS was employed to investigate the crystalline phases (Fig. 2 and SI Fig. S4.1-S4.4). The chosen representation in the waterfall plot may result in some peaks being less visible. However, it is important to emphasize that each peak was individually examined (SI Fig. S4.1).

Neat PCL, PDLA, multiblock copolymers P(PCL_{*m*}-*b*-PLLA_{*n*})_{*x*}, and their blends with PDLA_{*y*} were investigated. The WAXS diagrams revealed specific 2θ values for each constituent, which can correspond to homocrystallization of polylactide (PLA) in the form of α' crystals at 2θ values of 16.3° and 18.5° (110/200)⁴¹ or α crystals at 2θ values of 16.7°, 19.5° and 22.5° (203). Stereocomplexation between PLA and PDLA is represented at 2θ values of 12.4°, 20.8° and 24° (110/300/220) while crystallization of poly(ϵ -caprolactone) gives peaks at 2θ values of 22° and 24° (110/200) as shown in Fig. 3.^{29,41,42} In addition to the identification of the crystallite species, the relative crystallinities of the individual components were calculated by dividing the integral of the respective peak by the total integral area (eqn (8)) In contrast to metals and ceramics, polymers show semi-crystalline behavior and, therefore, show an amorphous background in scattering experiments, which leads to additional interference and decrease the signal to noise ratio resulting in a low sensitivity to vast, barely ordered ("amorphous") domains.⁴³ Nevertheless, WAXS is a widely established technique for identifying crystallite phases^{44,45} and estimating crystallite sizes even in polymeric materials.⁴⁶⁻⁴⁸

Crystallite sizes can be extracted from WAXS data using the Scherrer equation or by more advanced approaches such as the Williamson-Hall method, which also accounts for strain and lattice defects but is considerably more difficult to perform. Raman spectroscopy can also be used to estimate crystallite sizes; however, it requires a prior calibration using reference samples of known size, which is particularly challenging in the case of polymers—and even more so for multiblock copolymers (MBCs).⁴⁹ The Scherrer equation assumes isotropic (typically spherical) crystallites, while polymer crystallites are often lamellar, needle-like, or elongated. As a result, the method provides only approximate values and yields a single average crystallite size without information on structure, orientation, or amorphous fractions. However, due to its simplicity and the fact that it does not require correction for microstrain, it remains a widely used and practical tool for estimating domain sizes in polymer science. Especially for materials with complex morphologies such as semi-crystalline PLA/PCL systems, it is advisable to combine complementary techniques (e.g., WAXS with TEM or AFM) to gain a comprehensive understanding. Although we performed SAXS measurements on our samples,



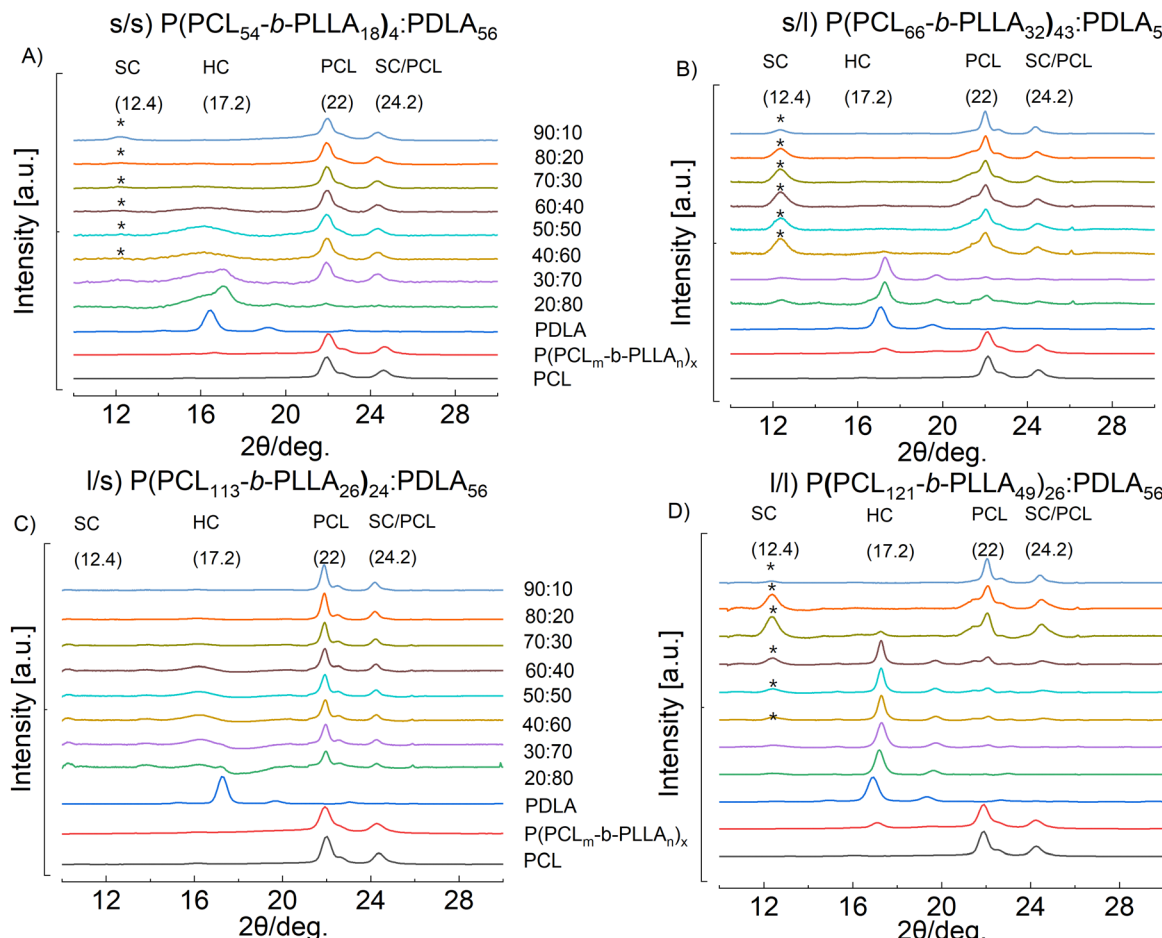


Fig. 2 WAXS diffractograms of PCL, PDLA homopolymers, $P(PCL_m-b-PLA_n)_x$ MBCs, and $P(PCL_m-b-PLA_n)_x:PDLA_{56}$ blends. (A) $P(PCL_{54}-b-PLA_{18})_4:PDLA_{56}$ (s/s), (B) $P(PCL_{66}-b-PLA_{32})_{43}:PDLA_{56}$ (s/l), (C) $P(PCL_{113}-b-PLA_{26})_{24}:PDLA_{56}$ (l/s), and (D) $P(PCL_{121}-b-PLA_{49})_{26}:PDLA_{56}$ (l/l). Some spectra have been normalized in order to make the intensity with the more intense peaks comparable. * indicates compositions, in which SC's were detected.

they did not yield interpretable results due to insufficient electron density contrast between the components. Given that the focus of this study was on the identification of crystalline domains and phase composition, WAXS and complementary techniques were prioritized, as they provided more relevant structural information. Therefore, the crystallite sizes or the size of the crystalline domains were calculated with the

Scherrer equation (eqn (9)) for the MBCs and blends (Fig. 3). The crystallite size analysis derived from WAXS patterns revealed a clear dependence on the segment length of the multiblock copolymers. As shown in Fig. 3, increasing PCL and PLLA block lengths resulted in a gradual growth of both homocrystallite of PCL and stereocomplex (SC) domains. For $P(PCL_{54}-b-PLA_{18})_4:PDLA_{56}$ (s/s), average PCL crystallite sizes

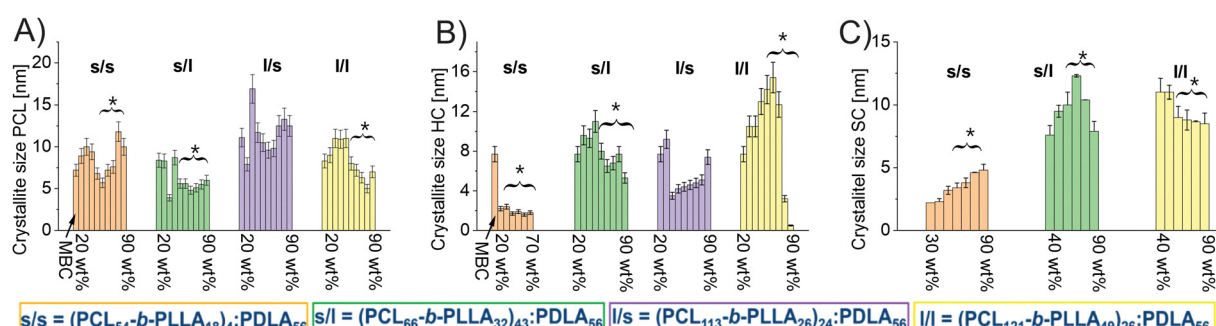


Fig. 3 Calculated crystallite sizes from the WAXS data of (A) PCL, (B) PLAHC and (C) PLA SC in $P(PCL_m-b-PLA_n)_x:PDLA_{56}$ blends. * indicates compositions, in which SC's were detected.



ranged from approximately 6–10 nm, whereas $P(PCL_{113}-b-PLLA_{26})_{24}:PDLA_{56}$ (l/s) and $P(PCL_{121}-b-PLLA_{49})_{26}:PDLA_{56}$ (l/l) exhibited larger domains of about 10–15 nm. A similar trend was observed for PLLA-HC and SC crystallites (Fig. 3B and C), indicating that longer segments provide greater chain mobility and packing regularity during crystallization. The observed increase in crystallite size with block length directly supports the proposed structure–property relationship, linking molecular architecture to crystalline domain size and phase formation.

3.2.1. Stereocomplex formation depends on PCL segment length. Results demonstrated that the block length from the PLA sequence length is not the only determining factor for the formation of SCs, the block length of poly(ϵ -caprolactone) (PCL) significantly influences the ability to form stereocomplexes, and no SC formation was observed in the combination of long PCL blocks with short PLA blocks l/s (Fig. 2C). All other block combinations s/s (A), s/l (B), and l/l (D) are able to form stereocomplexed PLA, as indicated by WAXS peaks at 12.4°, 20.8 and 24° (110/300/220). The formation of SCs took place not only in the typical 1:1 ratio between PLLA and PDLA, but also in mixtures with a ratio of up to 1:4, which disclosed that SCs can also be formed under conditions with an excess of one component. PDLA:PLLA stereocomplexes form archetypically at a 1:1 ratio,⁵⁰ though at other ratios, the 1:1 fraction may form the stereocomplexes, and even stereocrystallite structures with an excess of one component are known (up to 70:30 of either component).⁵¹

The inability of the PLA sequences in the l/s MBCs to crystallize may be explained by the vast block length difference, which leads automatically to a simultaneous reduction of wt% content of PLLA in the polymer, and which is only ~13 wt% in the l/s MBC. Interestingly, no SC formation occurs in any of the blends, though the blends contain at least 21 wt% PLA, and some of the other samples containing similar amounts of PLA show PLA crystallization (either HC or SC). A potential explanation may be derived from a visualization of microdomain formation. In MBCs, the PLLA and PCL sequences are covalently linked, and hence in case of phase separation of the blocks may lead to smaller domains than in a putative blend. Furthermore, it can be expected that on the interface between two domains there may be some co-localization of PCL and PLLA segments, potentially forming a mixed amorphous phase, as is sometimes observed in P(CL-co-LA) copolymers²⁶ and further reducing the size of a pure PLLA domain. When forming the blends with PDLA such PLLA segments might not be available for SC formation (see also below Section 4.8 “overall model”). Crystallizability by annealing was not investigated for these samples, but spontaneous crystallite formation in MBCs with vastly different block length during solvent evaporation seem to be inhibited.

According to Tsuji *et al.* stereocomplexation and homocrystallization are competitive processes and SC formation is preferred over HC formation when the molar mass is low, due to increased mobility of segments.⁵² This phenomenon is clearly visible in $(P(PCL_{54}-b-PLLA_{18})_4:PDLA_{56})$ in comparison to $P(PCL_{113}-b-PLLA_{26})_{24}:PDLA_{56}$, in which no diffraction peaks of

PLA-HC are visible, but diffraction peaks of SC at 12.4, 20.8 and 24° can be observed for the 90/10 mixture.

3.2.2. Two types of PLA HCs are formed. Four types of PLA crystallites (in the following referred to (HC) of PLLA or PDLA) are known: α' , α , β and γ .⁵³ PLA α -form crystals grow *via* solution, melt, or cold crystallization at high temperatures (*i.e.*, above 120 °C) in a 10/3 helical confirmation packed in an orthorhombic unit cell. The α' crystals are formed from the melt or by cold crystallization at temperatures below 100 °C and are similar though more disordered compared to the α form. Di Lorenzo *et al.* pointed out that the α form provides a better barrier to water vapor, a higher Young's modulus, and a lower elongation at break compared with films containing the α' modification.⁵⁴ α and α' type crystals may occur simultaneously in a sample, however, the transition $\alpha' \rightarrow \alpha$ is irreversible. The other crystal forms, *i.e.* the β - and γ -forms, of PLA grow under specific processing conditions that are not relevant to this work, and all of them tend to transition to the α form during heating.^{55,56}

The homocrystallization of PLA was not observed in the l/s MBC without blending. In comparable diblock copolymers, PLA crystallization was observed already in PLA sequences with molar masses ≥ 964 g mol⁻¹, corresponding to ≥ 13.4 lactide (LA) repeating units.²⁰ The WAXS graphs exhibit a peak at 17.2° indicating partial crystallization of HC as α -phase (ordered α crystal). In the PDLA_y's used for blending, the distorted α' -phase (16.3°) as well as α phase (19.4°) could be observed. The PDLA_y's used in the mixtures exhibited a high crystallization ability with relative crystallinities of 80% and crystallite sizes of 8 ± 1 nm. These crystallites are composed mainly from α' type crystallites (~80%) and ~20% α form. After blending the MBCs with PDLA, mixtures with a high proportion of PDLA (20/80) exhibit sharp HC crystallization peaks, which slowly decrease in intensity with increasing MBC content. These HCs are likely to be attributed to the PDLA content only (see discussion further below in the section on DSC). The HC in the blends mainly show an α phase with a small proportion of α' . When SC formation takes place, visible due to the peaks at 12° and 24°, the HC crystallization peak disappears (*e.g.* Fig. 2B 50:50). In the process of blending with PDLA₅₆, SC formation is preferred compared to HC formation and the overall relative crystallinity decreases until only crystallinities of about 5% remain. The overall HC crystallite sizes show a decrease with decreasing PDLA content. In the MBC's blends where no SC's are formed, either homocrystallization is visible, *e.g.* in $P(PCL_{121}-b-PLLA_{49})_{26}:PDLA_{56}$ (Fig. 2D 30:70), or polylactide forms predominantly an amorphous phase which may contain a very minor amount of HC (<10%) in the mixture (Fig. 2C 30:70).

In the blends prepared with PDLA₂₉ or PDLA₁₅, HC formation was visible in more compositions than with PDLA₅₆. This may suggest that the rearrangement of the longer chains of PDLA₅₆ may be sterically and/or kinetically hindered in the blends. Additionally, it is noticeable that homocrystallization is less favorable compared to stereocrystallization, as evidenced by the disappearance or reduction of the homocrystallites peak



compared to that of the stereocrystallites (e.g. for $P(PCL_{54}-b-PLLA_{18})_4:PDLA_{56}$).

3.2.3. PCL crystallization is generally reduced at high PLA content, though PLA crystallites may act as nucleation points.

The measured poly(ϵ -caprolactones) PCL_{54} , PCL_{66} (short) and PCL_{113} or PCL_{121} (long), exhibited a semi-crystalline behavior, displaying crystallite peaks of PCL in both the pure PCL (black line) as well as in the pure MBC (red line) (Fig. 2 and 3C). The calculated crystallite sizes were 7.2 ± 1 nm for PCL_{54} and PCL_{66} , and 11.3 ± 1 nm for PCL_{113} and PCL_{121} . Interestingly, the crystallite size of PCL in MBCs increased to 9 nm for $P(PCL_{54}-b-PLLA_{18})_4$. No change could be observed for $P(PCL_{66}-b-PLLA_{32})_{43}$ and $P(PCL_{121}-b-PLLA_{49})_{26}$, while crystallite size decreased from 11 nm in the individual PCL to 8 nm in $P(PCL_{113}-b-PLLA_{26})_{24}$.

PCL crystallization in the blends depended significantly on the block length of PCL_n and the corresponding length of the blended $PDLA_y$ as well as $PLLA_n$ length in the MBC. The l/l blends of $P(PCL_{121}-b-PLLA_{49})_{26}:PDLA_{56}$ show no crystallization of PCL up to a mixing ratio of 60/40 (Fig. 2D), but the blends l/s of $P(PCL_{113}-b-PLLA_{26})_4:PDLA_{56}$ exhibit crystallization of PCL in all blends (Fig. 2C). Comparing l/l blends with the PDLA of different lengths show PCL crystallization but for shifted compositions (see Fig. 2D and SI S4.3 and S4.4D). The reason for this could be that the crystallization of PCL in l/l is sterically hindered due to PDLA and the confinement through phase separation.

With the addition of PDLA to $P(PCL_m-b-PLLA_n)_x$ and the formation of stereocomplexes, a general decrease in the crystallite sizes of PCL compared to the pure PCL's was observed for s/l $P(PCL_{66}-b-PLLA_{32})_{43}$ and l/l $P(PCL_{121}-b-PLLA_{49})_{26}$ (Fig. 2B and D). In the blends based on MBCs with short lactide sequence length ($P(PCL_{54}-b-PLLA_{18})_4$ and $P(PCL_{113}-b-PLLA_{26})_{24}$), however, a slight increase or no change in PCL crystallite size is observed after stereocomplexation for the blends with $PDLA_{56}$ (Fig. 2A and C). The largest crystallite size of PCL, which was achieved in $P(PCL_{113}-b-PLLA_{26})_{24}:PDLA_{56}$, was around 20 nm. There is no data conveying how large the crystallites of PCL can become in multiblock copolymers with PLLA. Castilla *et al.*, however, disclosed that PCL crystallite sizes can grow up to 22 nm by using graphene oxide (GO) filler as an nucleation agent in PCL films.⁵⁷ Even though they used PCL (M_w 90–150 kDa) combined with a nucleation agent, the crystallite sizes achieved are comparable to our case. Crystal growth depends on the length of the molecular chain and its freedom to fold.⁵⁸ Therefore, it can be assumed that the growth rate of the PCL nucleation sides is decreased due to the constrained geometry, caused by attached PLLA segments, their length and their prior crystallization. The well-known immiscibility of PCL and PLLA⁵⁹ further leads to lower diffusion rates of the PCL polymer chains in the already crystallized PLA domains and promotes disordered crystallization, hence smaller crystallites and lower relative crystallinities. This inhibition of PCL crystallite formation was also found by other groups.²⁰

3.2.4. Crystallite sizes tend to correlate with block sizes.

The SC crystallite size found in the $P(PCL_m-b-PLLA_n)_x:PDLA_{56}$ blends were between 5 and 13 nm. The largest SC crystallites of ~ 13 nm in this series were found in the s/l $P(PCL_{66}-b-PLLA_{32})_{43}$ and l/l $P(PCL_{121}-b-PLLA_{49})_{26}$ MBCs (Fig. 2C). However, the

difference between 32 and 49 repeating units of PLLA in terms of maximum SC crystallite sizes was within the margin of error. The majority of samples, especially with shorter PDLA components, contains SC crystallites with a size between 6–9 nm, and as small as < 1 nm for $P(PCL_{66}-b-PLLA_{32})_{43}:PDLA_{15}$.

3.2.5. Stereocrystallization strongly influences PCL and PLA HC crystallization.

The crystallization of PCL was promoted in mixtures where SCs were formed, indicating that the formation of SCs acted as a nucleating agent for the crystallization of other components, though one needs to take into consideration also that the wt% content of PCL in the mixture increases (e.g. Fig. 2D 80 : 20). In mixtures where no SCs were formed, the crystallization of PCL was inhibited. The crystallite sizes and relative crystallinity of HC tended to decrease when SCs were formed, as the PDLA is used for SC formation. All crystallite sizes determined were between 2 and 15 nm.

The work of Chengbo *et al.* has demonstrated that the crystallite sizes of PLA can vary significantly. In their study, the PLA crystallite sizes started at around 8 nm. With increasing temperature and under uniaxial loading, these sizes increased up to 20 nm. This indicates that the thermal and mechanical conditions have a significant influence on the microstructure of the material.⁶⁰ The crystallite size of PLA in PLA/clay nanocomposite films were around 14 to 19 nm.⁶¹ There, clay was used as a nucleation agent to enhance the crystallization behavior of PLA. We detected similar crystallite sizes ranging from approximately 5 nm to 23 nm for HC in blends with $PDLA_{56}$ (Fig. 3B). We found the highest HC crystallite sizes in the $P(PCL_{121}-b-PLLA_{49})_{26}:PDLA_{15}$ (~ 20.0 nm) 90 : 10, $P(PCL_{121}-b-PLLA_{49})_{26}:PDLA_{29}$ (~ 22 nm) 70 : 30 and $P(PCL_{121}-b-PLLA_{49})_{26}:PDLA_{56}$ (~ 22.4 nm) 60 : 40 blends. The lowest PLA crystal sizes were found in $P(PCL_{66}-b-PLLA_{32})_{43}:PDLA_{15}$ (~ 1 nm) 20 : 80, $P(PCL_{113}-b-PLLA_{26})_{24}:PDLA_{56}$ (~ 2.2 nm) 20 : 80 and $P(PCL_{54}-b-PLLA_{18})_4:PDLA_{15}$ (~ 2 nm) 20 : 80 blends. The results indicate that the crystallite size of PLA homocrystallites is primarily governed by the length of the PLLA segments within the multiblock copolymer rather than by the molecular weight of the PDLA blending component. Longer PLLA blocks facilitate more efficient chain folding and lamellar thickening, leading to the formation of larger and more ordered HC domains. In contrast, shorter PLLA segments restrict chain mobility and limit the growth of crystalline lamellae, resulting in smaller crystallites. This suggests that the crystalline structure in these blends is mainly dictated by the intrinsic block architecture of the MBC rather than by the composition of the PDLA phase, highlighting the dominant role of PLLA segment length in determining the microstructural organization of the blends. Crystallite sizes of in $P(PCL_m-b-PLLA_n)_x:PDLA_{56}$ are in the range of 1–20 nm regardless of whether it is PCL, HC or SC. Since the measurements were performed on samples after processing without annealing, this crystallite formation depends primarily on the kinetics of nucleation and crystallite growth strongly influenced by sequence lengths, molar mass, and viscosity of the solution.

3.3. Crystallinity and thermal behavior

Thermal transitions of the synthesized PCL's, PDLA's, $P(PCL_m-b-PLLA_n)_x$ multiblock copolymers and their mixtures with



Table 2 Thermal transitions and crystallinities obtained from DSC scans of PCL homopolymers and $P(PCL_m-b-PLLA_n)_x$ multiblock copolymers

Material	PCL				PLA			
	T_m (°C)	T_c (°C)	ΔH_m (J g ⁻¹)	X_c (%)	T_m (°C)	T_c (°C)	ΔH_m (J g ⁻¹)	X_c (%)
PCL ₅₄ /PDLA ₁₅ ^a	59	28	111	78	125	81	48.8	51
PCL ₆₆ /PDLA ₂₉ ^a	63	30	112	79	140	89	59.5	64
PCL ₁₁₃ /PDLA ₅₆ ^a	60	31	111	78	158	105	72.8	78
PCL ₁₂₁	58	31	100	70	—	—	—	—
$P(PCL_{54}-b-PLLA_{18})_4$	62	28	69	61 ^b /78 ^c	101	—	1.7	2 ^b /6 ^c
$P(PCL_{66}-b-PLLA_{32})_{43}$	55	37	72	54 ^b /79 ^c	117	68	4	4 ^b /9 ^c
$P(PCL_{113}-b-PLLA_{26})_{24}$	63	27	104	63 ^b /78 ^c	—	—	—	—
$P(PCL_{121}-b-PLLA_{49})_{26}$	60	18	79	62 ^b /70 ^c	123	—	3	3 ^b /8 ^c

^a Individual PCL or PDLA samples. ^b Absolute crystallinity of PCL in $P(PCL_m-b-PLLA_n)_x$ multi-block determined by DSC. ^c Relative crystallinity of PCL in $P(PCL_m-b-PLLA_n)_x$ multi-block determined by DSC.

PDLAs were determined by DSC (Table 2). Data from the first heating and cooling (both at 10 K min⁻¹) were used as this describes the material properties after film formation (Fig. 4 and S5.1–5.2, S6.1–6.3). This is relevant to a potential application and is more consistent for a comparison with WAXS data than using the second heating experiments. Results from selected annealing experiments are also be presented below. The glass transition temperature (T_g), melting temperature (T_m) and crystallization temperature (T_c) were determined from the

measurements, and the absolute and relative crystallinities were calculated using the eqn (5)–(7).

The thermograms show three specific melting regions, the peaks of PCL (58–63 °C), PLA HC (140–180 °C) and SC (170–200 °C). Verification of the assignment as HC or SC melting was done by comparison with the WAXS data of the individual sample (Fig. 3). Additionally, cold recrystallization (90–120 °C) occurred, which marks the reorganization from the α' to the α phase during heating.

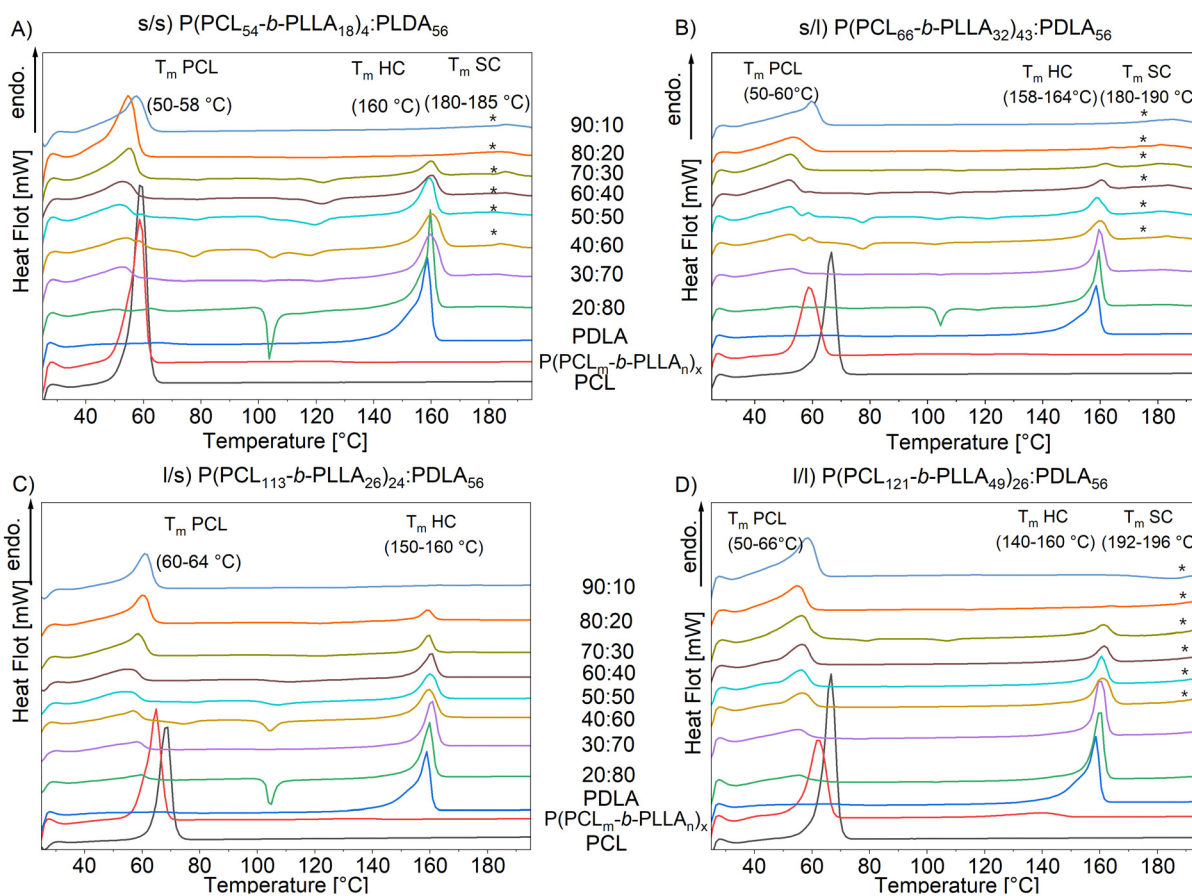


Fig. 4 DSC thermograms of $P(PCL_{54}-b-PLLA_{18})_4$:PDLA₅₆ (A), $P(PCL_{66}-b-PLLA_{32})_{43}$:PDLA₅₆ (B), $P(PCL_{113}-b-PLLA_{26})_{24}$:PDLA₅₆ (C) and $P(PCL_{121}-b-PLLA_{49})_{26}$:PDLA₅₆ (D) obtained at heating rates of 10 K min⁻¹. Asterisks indicate melting transitions consistent with SCs.

3.3.1. Relative crystallinity of PCL is independent from the presence of PLA. The relative crystallinity of PCL in the multi-block copolymers is comparable to that in the single PCLs. The absolute crystallinity is lower, due to the lower PCL content after addition of PLLA. In general, the total absolute crystallinity was found not to exceed 50% during isothermal heating. It was observed that for longer PLLA segments (> 26) in the MBCs, the melting temperature of PCL is represented by a double endothermic peak, indicating two different crystalline domains.

The melting temperatures (T_m) for PCL range from 58 to 63 °C and has a maximum for PCL₆₆ (black line in Fig. 4). The corresponding heating curve illustrates a single endothermic peak and shows that a single crystal phase is present in the pure PCL, probably facilitated by a low dispersity.

The calculated crystallinity of the synthesized caprolactones is around 70–80% for the synthesized PCLs. Boyd established the conceptual framework distinguishing between crystal mobile and crystal-fixed polymers, linking the chain mobility during crystallization to the achievable degree of crystallinity.⁶² Additionally, Thurn-Albrecht *et al.* demonstrated that PCL behaves as a crystal fixed polymer; when crystallized from the melt, it cannot exceed a crystallinity of $\sim 60\%$.^{63,64} However, in our case, solution-based processing enables slower crystallization and more favorable chain organization, allowing higher relative crystallinities than are usually observed from the melt.^{65–67}

The slightly lower crystallinity of PCL₆₆ in P(PCL₆₆-*b*-PLLA₃₂)₄₃ compared to the other samples corresponds with the lower melting temperature, suggesting smaller crystallite sizes. This highlights the common occurrence that there is an optimum chain length for crystallization, which first increases with molar mass but at some stage drops again as then entanglements and lower chain mobility reduce crystallizability.⁶⁸

3.3.2. There is no clear correlation between PCL chain length and crystallinity. There are slight changes in the T_m of the PCL in the MBCs compared to the individual PCL, with a notable decrease for P(PCL₆₆-*b*-PLLA₃₂)₄₃. Here, the ability to form crystalline regions is reduced by the introduction of other blocks in the copolymer, which can disrupt the regular packing of the PCL chains. This disruption leads to a decrease in the

overall relative crystallinity and crystallite size (WAXS data Fig. 2B) of the PCL segments. As a result, the corresponding melting temperature is lowered.

The T_m of PCL in the blends is represented by a double endothermic peak when the MBC part has long PLLA segments (> 26), suggesting two different crystalline domains. This low double melting peak has been explained in low molar mass PCL's ($< 10 \text{ kg mol}^{-1}$) by partial melting and reorganization during the heating scans.⁶⁸

The relative crystallinity of PCL changes depending on the MBC and blend composition. In most samples the relative crystallinities decrease after blending with PDLA₅₆. Particularly in the mixtures of *e.g.* P(PCL₆₆-*b*-PLLA₃₂):PDLA₂₉ 20/80, their relative crystallinity is decreased from 80 to 49% (not shown). The absolute crystallinity is decreasing from 53 to 4%. However, in some samples, interestingly the relative crystallinity increases *e.g.* in P(PCL₁₂₁-PLLA₄₉)₂₆:PDLA₅₆ from 82% to 98% and in P(PCL₆₆-PLLA₃₂)₄₃:PDLA₅₆ from 80% to nearly 100% in the 30:70 blend (Fig. 5A). The blends exhibit lower relative crystallinities at higher MBC content. The absolute crystallinity of PCL obviously increases because of the higher mass fraction. Of note is that in blends that allow SC formation, the highest PCL crystallinity coincides with the presence of SCs (*cf.* Fig. 5A and B).

3.3.3. Cold crystallization occurs in several blends, linked to PCL content. A cold crystallization peak around 90 to 110 °C was detected in the first heating run of several blends, to be exact in P(PCL₅₄-*b*-PLLA₁₈)₄:PDLA_{56/30}, P(PCL₆₆-*b*-PLLA₃₂)₄₃:PDLA_{56/15} and P(PCL₁₁₃-*b*-PLLA₂₆)₂₄:PDLA₅₆ (Fig. 5A–C). As has been shown before, formation of SCs is strongly dependent on molar mass and temperature,^{41,45} and that if one component has a molar mass $< 10^4 \text{ g mol}^{-1}$, SC formation is dominating.⁶⁹ However, in the studied system, this cold crystallization peak can be attributed to the recrystallization of the α' phase to the more stable α phase^{70,71} as it also occurs in systems that do not exhibit SC according to the WAXS investigations. The enthalpy of cold crystallization of PLA increases with increasing PCL content. This is likely since PCL can sterically hinder PLA crystallization during solution casting, which is partially overcome by the increased chain mobility at increased temperatures that are above T_g of PLA and the T_m of PCL.

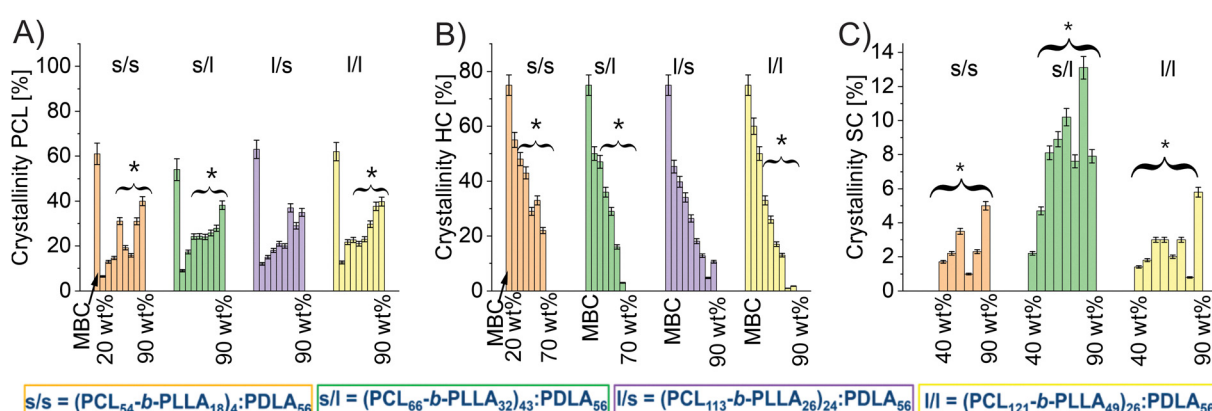


Fig. 5 Absolute crystallinities of (A) PCL, (B) PLA HC, and (C) PLA SC in the P(PCL_m-*b*-PLLA_n):PDLA₅₆ blends calculated from DSC experiments.



3.3.4. Stable HC melting temperature with increasing MBC content until consumption. The melting temperature of the pure PDLA₅₆ used for the mixtures with MBCs is 157 °C and PDLA₅₆ displays an absolute crystallinity of 66%. PLA HCs in the blends have similar melting temperatures, and considering blend compositions with high PDLA content, these are most likely to be attributed to PDLA homocrystallization. This suggests that the crystallite size of PDLA remains about the same upon blending. As rationale, in contrast to the PLLA segments that are covalently linked to PCL, the PDLA/phase separation seems to be clearer with smaller mixed interphase areas. The absolute crystallinity of PDLA decreases with decreasing PDLA content (Fig. 5B). In the 80/20 blend that contains a major amount of SC, the lowest relative crystallinity of HC is about 4%. However, the relative crystallinity of PDLA can even increase up to 75% in the blends compared to the pure PDLA, such as is the case *e.g.* for P(PCL₁₂₁-*b*-PLLA₄₉)₂₆:PDLA₅₆ 20/80.

3.3.5. The relatively low T_m of SCs indicate small crystallite sizes. The melting temperature of the stereocrystallites was in the range of 180 °C to 200 °C. This is significantly lower than in systems studied to maximize stereocrystallization, where the melting temperature of stereocrystallites was in the range of 200 to 230 °C.⁷² There are works where this was even exceeded, for example Ikada *et al.* found melting temperatures of 239 °C after aging for three years,⁵² and under stretching Wang *et al.* detected it at 240 °C.⁷³ In our system and comparable ones SC crystallites seem to be smaller leading to lower melting temperatures,^{26,27} though still significantly higher than *e.g.* shown in stereo-periodical copolymers based on P(LLA-LLA-DLA) and P(DLA-DLA-LLA) (143.4–144 °C).⁷⁴

The melting temperatures of stereocrystallites in P(PCL₅₄-*b*-PLLA₁₈)₄:PDLA₅₆ and P(PCL₆₆-*b*-PLLA₃₂)₄₃:PDLA₅₆ blends were in the range between 180 and 190 °C. Higher melting temperatures in the range of 190–200 °C were achieved for the P(PCL₁₂₁-*b*-PLLA₄₉)₂₆:PDLA₅₆ samples. This suggests that larger crystallites are present in P(PCL₁₂₁-*b*-PLLA₄₉)₂₆:PDLA₅₆, which could be due to longer sequence lengths of PLLA. The crystalline content of stereocomplexes in the multiblock copolymer mixture with PDLA increases with increasing PLLA content in the MBC. The absolute crystallinities range between 2% for P(PCL₆₆-*b*-PLLA₃₂)₄₃:PDLA₅₆ (40/60) and 13% P(PCL₆₆-*b*-PLLA₃₂)₄₃:PDLA₅₆ (90/10). The blends corresponding to a 1:1 mixture of PLLA and PDLA showed the highest absolute crystallinity. There was no clear trend regarding the relative crystallinities and blend compositions. In general, the total absolute crystalline content, which was achieved by isothermal heating experiments (see below), didn't exceed 50% (crystallinity PCL + crystallinity SC + crystallinity HC).

3.4. Change in crystalline phases by annealing

The studies unveiled that thermal post-treatment (annealing) of P(PCL_{*m*}-*b*-PLLA_{*n*})_{*x*}:PDLA₅₆ blends can influence the crystal structure and relative crystallinity. While the slow solvent evaporation process tends to promote the formation of HC, annealing can transform less ordered α' -crystals into more ordered α -phases and finally into SC. This conversion was particularly observed in samples with a higher content of PCL

and a large difference in the block length of the enantiomers. On the other hand, in samples with a 50:50 ratio of MBC to PDLA₅₆, the relative crystallinity and crystal size remained largely unchanged, indicating the limited ability to form SCs under these conditions. In samples with a 90:10 ratio of MBC:PDLA₅₆, the crystal size could be increased from 4 to 12 nm by annealing, while the relative crystallinity showed a slightly increase from 20 to 25%.

It has been reported that the stereocomplex crystal formation can be controlled by the diffusion of the enantiomeric chains.⁷⁵ Therefore, the length of sequences forming the homocrystallites and the control of chain mobility in the processing method is crucial for achieving SC formation. In solution casting processes many parameters can affect crystallization *e.g.* the concentration of the polymer in the solution or the evaporation rate of the solvent.⁷⁶ In melt based processes, the M_w and the melting temperature are the main driving forces. Pengju's group⁷⁵ confirmed that after rapid solvent evaporation SC formation was exclusively achieved compared to slow solvent evaporation, which was attributed to simultaneous folding of PLLA and PDLA chains. Since film casting and, therefore, SC formation were performed under slow solvent evaporation for our samples, the crystallization might be shifted towards HC formation. Therefore, annealing was performed on selected samples to see whether it influences crystallite structure and relative crystallinity. Fig. 6 displays WAXS profiles of P(PCL₆₆-*b*-PLLA₃₂)₄₃:PDLA₅₆ blends of two compositions (50:50/90:10), which were annealed at T_c = 190 °C, T_c = 120 °C and room temperature (Table S1 gives crystallite sizes and crystallinities). Each temperature was maintained for 200 minutes, to give the crystallites sufficient time to grow. Afterwards, the wide-angle scattering profiles from the samples were determined at room temperature (approximately 25 °C) (Fig. 6). The crystal formation during the annealing process was observed *via* POM.

Although PLA is known to degrade thermally over 200 °C, the annealing conditions were carefully selected based on prior reports on stereocomplex formation, which require complete melting of homocrystallites and enhanced chain diffusion. No significant degradation was observed under these conditions, as verified by TGA analysis indicated no appreciable mass loss during the treatment, confirming the thermal stability of the material under our specific protocol. In the 90:10 MBC:PDLA blend, annealing led to a shift from HC to SC, growth of SC crystallite sizes, and an increase in relative PCL crystallinity. Indeed, this suggests that the slow solvent evaporation used in our system supports HC formation, while annealing allows chain re-organization promoting the thermodynamically more stable SC phase. In the 50:50 mixture however, no changes in relative crystallinity or crystallite sizes were observed upon annealing, and the relative crystallinity of SCs was only in the 7–10% region. Likely, the relatively high PCL content and the phase separated structure doesn't allow for extended SC formation under the studied conditions.

3.5. Crystallite distribution

The investigation of the crystallite distribution in different (PCL_{*m*}-*b*-PLLA_{*n*})_{*x*} blends highlights that the crystallite structure



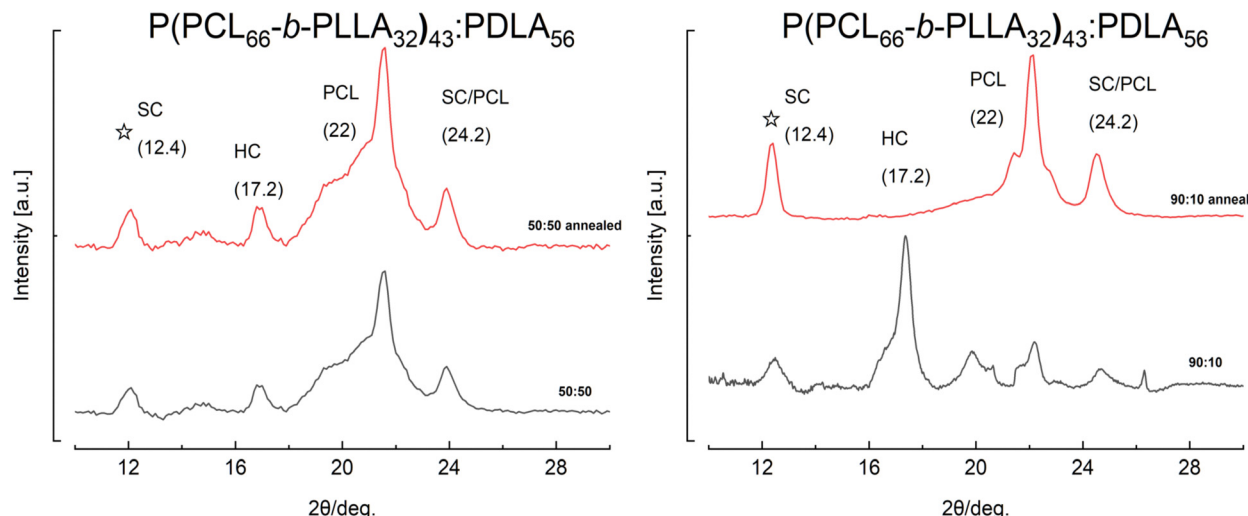


Fig. 6 $\text{P}(\text{PCL}_{65}-b\text{-PLLA}_{30})\text{:PDLA}_{59}$ annealed for ~ 120 minutes, by heating to $200\text{ }^\circ\text{C}$ hold at temperature for 1 minute, cool down to $190\text{ }^\circ\text{C}$ and hold for 30 minutes, cool down to $160\text{ }^\circ\text{C}$ and hold for 30 minutes, cool down to $130\text{ }^\circ\text{C}$ hold it for 10 minutes, cool down to $100\text{ }^\circ\text{C}$, $80\text{ }^\circ\text{C}$ (10 minutes) and cool down to RT. (A), $\text{P}(\text{PCL}_{66}-b\text{-PLLA}_{32})_{43}\text{:PLDA}_{56}$ 50 : 50 blend and (B), $\text{P}(\text{PCL}_{113}-b\text{-PLLA}_{26})_{24}\text{:PLDA}_{56}$ 90 : 10 blend.

strongly depends on the mixing ratio and the processing. Samples without stereocomplex formation showed large spherulitic structures, while samples with stereocomplexes revealed a clear phase separation and formed smaller sc-PLA crystallites. An increase in PCL content led to a decrease in PLA HC crystallite size, indicating inhibition of crystallization by PCL. AFM and WAXS confirmed the presence of crystalline lamellar structures in PLA HC and the formation of stereocomplexes in certain blends.

Furthermore, the results indicated that PCL can act as a physical barrier affecting both nucleation and growth of PLA crystallites.

Fig. 7 and 8 illustrate the phase structure of several $(\text{PCL}_m-b\text{-PLLA}_n)_x\text{:PDLA}_{56}$ blends. The phase structure was investigated using AFM and POM. In the POM image acquisition, the polymer films were additionally heated to $200\text{ }^\circ\text{C}$ in order to assign the different crystallites to the different components (SI Fig. S8.2).

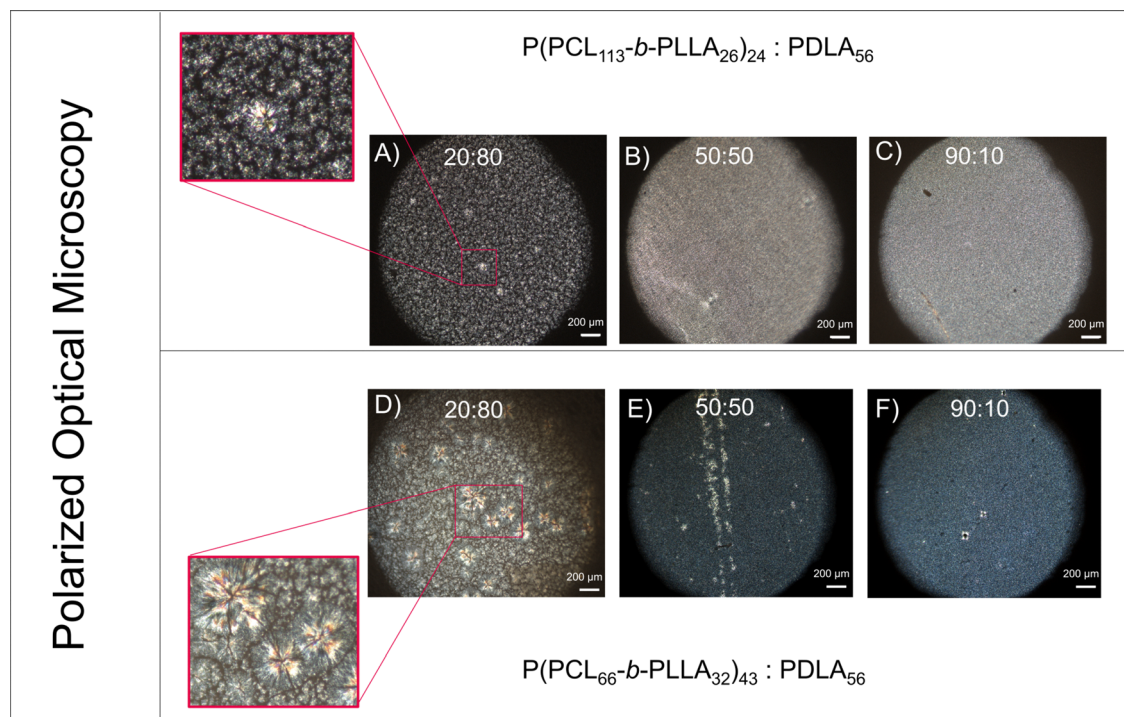


Fig. 7 Phase structure by polarized optical microscopy of $\text{P}(\text{PCL}_{113}-b\text{-PLLA}_{26})_{24}\text{:PLDA}_{56}$ blends upper row and $\text{P}(\text{PCL}_{66}-b\text{-PLLA}_{32})_{43}\text{:PLDA}_{56}$ blends lower row, taken from the polymer films. The following mixtures are displayed (A) and (D) 20 : 80, (B) and (E) 50 : 50 and (C) and (F) 90 : 10.



3.5.1. Crystallite morphology in blends is strongly influenced by the mixing ratio. Fig. 7(A)–(C) and 8(A)–(C) shows $P(PCL_{113}-b-PLLA_{26})_{24}:PDLA_{56}$, in which no stereocrystallization occurred, and $P(PCL_{66}-b-PLLA_{32})_{43}:PDLA_{56}$ (d–f) where SCs were formed. Fig. 8A, D and 9A, D reveal PLA HC forming large

spherulitic structures that appear as round, radial patterns under the microscope. These radial spherulitic structures are also known as Maltese cross spherulites and are common for PLA.^{44,77,78} These structures consist of many small, needle-shaped crystals radiating from a central nucleation point. The

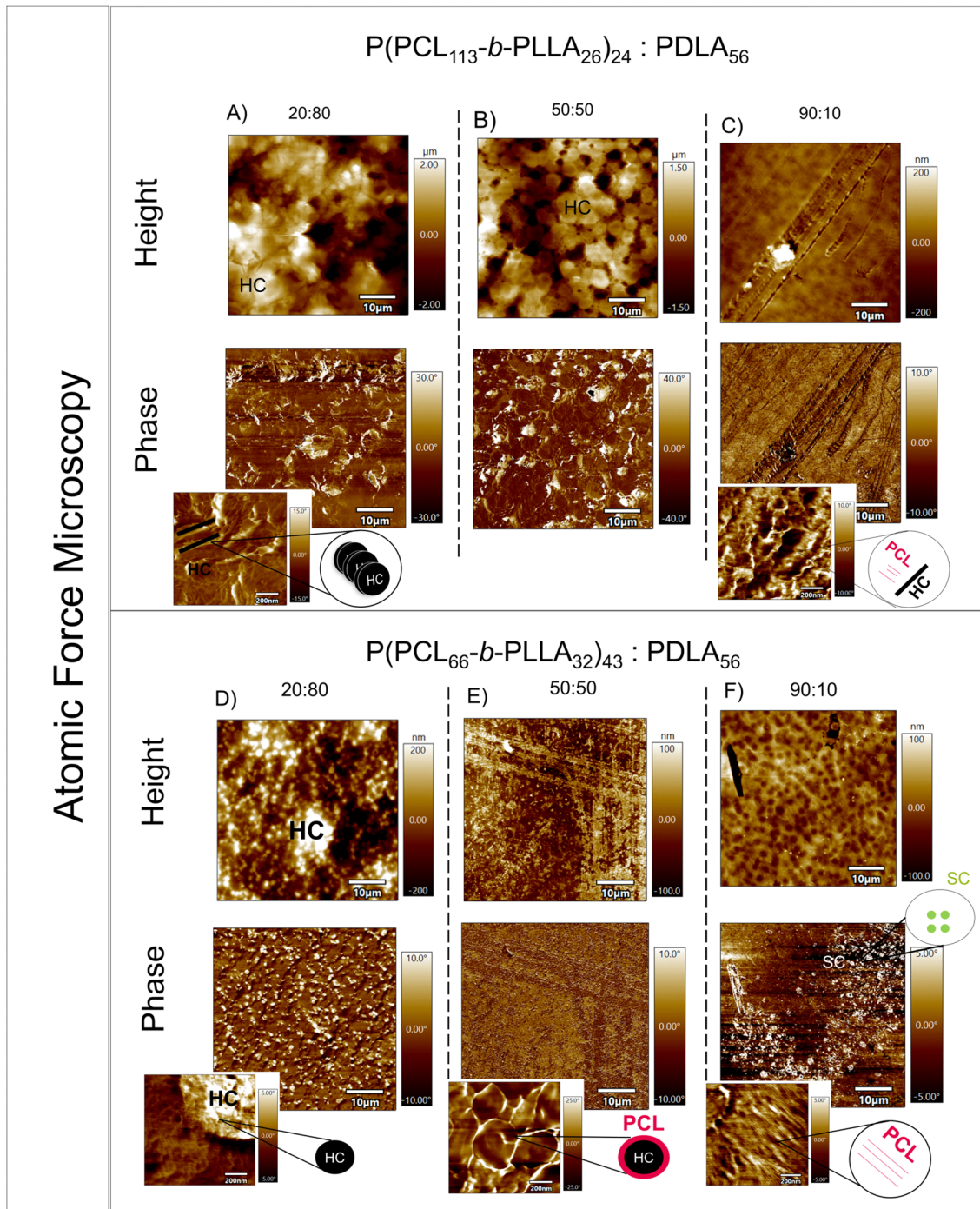


Fig. 8 Atomic force microscopy (AFM) images of two MBC blends, showing height and phase maps for three blend ratios (20 : 80, 50 : 50, and 90 : 10). For $P(PCL_{113}-b-PLLA_{26})_{24}$ (A)–(C), the height maps (top row) and corresponding phase maps (bottom row) illustrate the surface morphology and material property variations, respectively, for the three blend ratios. Similarly, for $P(PCL_{66}-b-PLLA_{32})_{43}$ with $PDLA_{56}$ (D)–(F), the height maps (top row) and phase maps (bottom row) show the structural and compositional characteristics for the same blend ratios. The images reveal how blending ratios influence the morphology and phase distribution within the samples.

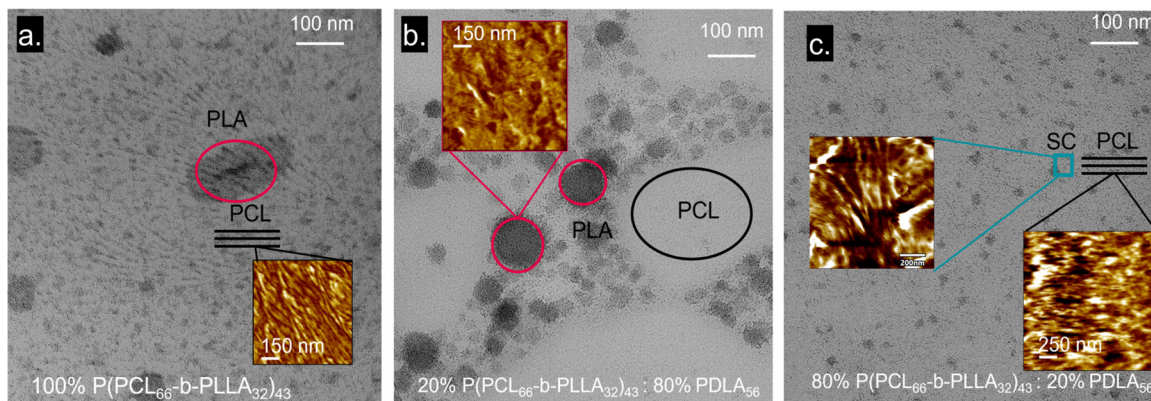


Fig. 9 TEM micrographs of (a) $\text{P}(\text{PCL}_{66}\text{-}b\text{-}\text{PLLA}_{32})_{43}$, (b) $\text{P}(\text{PCL}_{66}\text{-}b\text{-}\text{PLLA}_{32})_{43}\text{:PDLA}_{56}$ 20 : 80 and (c) $\text{P}(\text{PCL}_{66}\text{-}b\text{-}\text{PLLA}_{32})_{43}\text{:PDLA}_{56}$ 80 : 20.

agglomerates of crystallites are up to 100 μm in size. As Tsuji *et al.* have shown using polarized optical microscopy, crystalline spherulites of homocrystallites can be several 100 μm in size, which is consistent with our investigation.¹¹ The values determined from WAXS by the use of the Scherrer equation are much smaller, as there the size of the individual crystalline domains within a material are determined.

AFM height images show that in the PLA HC sample, the crystallites protrude from the surface, reaching heights of up to 250 nm (see Fig. 8A and D height). These crystallites are characterized by their lamellar structure, which forms radially around the nucleation point (Fig. 8A and D detail). The 90 : 10 MBC mixture $\text{P}(\text{PCL}_{113}\text{-}b\text{-}\text{PLLA}_{26})_{24}\text{:PDLA}_{65}$, where no SCs were formed, also exhibits a lamellar structure of PLA HC, which is visible in the AFM phase images (Fig. 8C). These structures crystallize into wave-like patterns at the ends of PCL lamellae and are distinctly different from the Maltese-cross shaped spherulites. The crystallites were assigned to PLA by heating experiments, as the crystallites melt in the range between 140–180 $^{\circ}\text{C}$.

3.5.2. Increasing PCL content restricts PLA HC spherulite formation. Fig. 7 and 8(B), (E), illustrate the 50 : 50 mixture and a highly phase separated structure with PLA crystals smaller in size compared to Fig. 7(A) and (D), of $\text{P}(\text{PCL}_{66}\text{-}b\text{-}\text{PLLA}_{32})_{43}\text{:PDLA}_{56}$ and $\text{P}(\text{PCL}_{113}\text{-}b\text{-}\text{PLLA}_{26})_{24}\text{:PDLA}_{65}$. Image 8D shows a more distinct phase separation and possibly a stronger crystallization, which is indicated by the uneven distribution of brightness. The size of the PLA crystallites decreases remarkably with increasing PCL content. PCL can act as a physical barrier and delay the nucleation of PLA crystallites. However, once nucleation takes place, PCL can still interfere with the growth of PLA crystallites by blocking access to the growing crystallite surfaces or hindering the necessary orientation of the PLA chains. Fig. 8E discloses a long crystal band, possibly formed by a combination of directional crystallization and phase-specific nucleation. The visualization of PCL crystallites and their aggregates was not possible by POM, even in combination with heating experiments, as the PCL crystalline/amorphous regions were to small and close to the PLA phases and, hence, PLA crystallites and their aggregates prevent a clear view on the PCL crystallites. This suggested a strong hierarchical crystallization, where PCL either

crystallizes between PLA phases or HC crystallites are formed on top of the PLA/PCL phase.^{44,77,78}

In samples with a higher MBC content in the blend (90 : 10), PCL and PLLA dominate the mixture. This generally leads to a finer distribution of the PLA phase, as it is present in smaller quantities and PLLA and PDLA cannot be differentiated. With a higher proportion of MBC, the crystallization of the PLA phase may be more inhibited, resulting in smaller crystallites and, thus, a finer microstructure, which is visible in the images. Fig. 8C (PLA HC) depicts the chain crystallization of PLLA and the orientation of the left-handed crystallites. For PLA SC depicted in Fig. 7F and 8F, small star-like crystallites are formed, which are connected by lamellar oriented PCL chains (Fig. 8F detailed). The experiments also show that around 180 $^{\circ}\text{C}$ crystalline structures are still present for the HC sample (see Fig. 8C) in contrast to the SC sample (see Fig. 8F). In addition, the WAXS data (Fig. 2) proves stereocrystallites in Fig. 8F and homocrystallization in Fig. 8C.

To our knowledge, in literature there is only a single reported observation of SC crystals in AFM tapping mode.⁷⁹ While the triclinic structure of the unit cell⁸ can be derived from the WAXS data according to the 2θ values of 12.4°, 20.8° and 24° (110/300/220), the SC crystals observed by AFM here did not have a well-ordered diamond-like shape. This can be explained by the fact that SC-crystallites are acting as nucleating agents for HC crystalline domains of the smaller PDLA component of the blend. The crystallites continue to grow until impinging to another PDLA spherulite. This leads to large spherulites of PDLA on top,⁸⁰ exactly the phenomenon we observed in our films, and that also has been proven by Chang *et al.* who investigated the crystallization and morphology of stereocomplexes in non equimolar mixtures of poly(L-lactic acid) with excess poly(D-lactic acid). In contrast SC's agglomerate in the form of small rod-shapes shown by the group of Dove for PHEAAm_y-b-PLLA_x (or PDLA_x-b-PHEAAm_y) triblock copolymers. They have demonstrated this for micelle-like structures, which are arranged in a spherical shape, and in star/octopus structures similar to our investigated materials.⁸¹

If we assume that stereocomplexes always form in a 1 : 1 ratio, then according to Watanabe *et al.* there are three ways in



which a long PLLA can mix with a short PDLA. Firstly, the lamellae of PLLA and PDLA orient themselves parallel to each other. Secondly, the lamellae are oriented parallel to each other, with the short PDLAs being in a row and crystallizing parallel to the PLLA, or thirdly, short PDLAs are wrapped by long PLLAs to form stereocrystallites. The AFM image strongly suggests that here variation 3 is present, as no regular crystallites are formed, and the presence of PCL further disturbs this order. Additionally, the group of Park was able to show similar SC crystallites in PLLA/PDLA blends.⁸²

3.6. Visualization of micro-and nanophase domains by TEM & AFM

In order to visualize the different crystal phases, the nano- and microphase-separated morphologies of $P(PCL_m-b-PLLA_n)_x$:PDLA₅₆ blends were studied by TEM and correlated with AFM on the same spot. Samples were prepared by drop casting on Cu TEM grids (700 mesh) and subsequent stained with RuO₄. The staining allows to differentiate between amorphous and crystalline phases as crystalline phases appear darker.^{83,84}

By the correlative characterization approach, using TEM, which can reveal crystal structures and defects in the depth of the sample, and AFM, which provides topographical maps and mechanical properties of the surface, we were able to investigate the different crystalline domains. Additionally, this investigation enabled us to compare whether the same crystallization kinetics are present in the cast films and the drop casted films and to help structure assignment in TEM images. In fact, in both sample preparation techniques comparable crystallization processes take place.

TEM images are shown in Fig. 9a and show that the pure $P(PCL_{66}-b-PLLA_{32})_{43}$ multiblock copolymer has a lamellar PCL morphology, which is disturbed by crystalline PLA islands. The addition of PDLA results in the growth of the PLA islands and adjacent PCL domains, which are highly amorphous. This indicates an inhibition of PCL crystallization and is consistent with the WAXS results.

3.6.1. Stereocrystallites are embedded in the semi-crystalline PCL matrix. In the blends where SC are formed, a finer phase image is seen which is similar to the microscopy images, with stereocrystallites embedded in a semi-crystalline poly(ϵ -caprolactone) matrix. AFM phase images confirm that the PLA-HC domains become smaller at higher MBC content, which is consistent with the WAXS data. By using TEM and AFM correlative, we were able to visualize and compare different crystalline domains, providing a comprehensive insight into the crystallization dynamics of the studied material. Fig. 9 the obtained TEM images of $P(PCL_{66}-b-PLLA_{32})_{43}$ (Fig. 9a) and as $P(PCL_{66}-b-PLLA_{32})_{43}$:PDLA₅₆ blends with 10 (Fig. 9b) or 90 wt% (Fig. 9c) MBC content.

The pure $P(PCL_{66}-b-PLLA_{32})_{43}$ MBC exhibited a lamellar morphology from semi-crystalline PCL and its parallel aligned PCL lamellas,⁸⁵ with darker PLA crystallites⁸⁶ distributed in the semicrystalline matrix. The assignment of PCL was achieved by comparison with AFM heating experiments up to 50 °C and POM/AFM measurements (previous section). The lighter areas

show that these are amorphous regions and confirm the semi-crystalline phase structure of the multiblock.

3.6.2. PCL lamellae crystallize in between SCs. After adding PDLA to the MBC, an increase in size of the lighter crystalline islands of PCL can be seen. This suggests that PCL crystallization is hindered, which is also supported by the WAXS data. As AFM phase imaging (inset of Fig. 9b) confirms, the Maltese cross like structures correspond to crystalline PLA domains. With increasing MBC content, the PLA phase domains get significantly smaller from around 100 nm to 10 nm, which fits to the smaller crystal sizes determined from WAXS data. Nevertheless, WAXS revealed only SC and PCL crystallites in the displayed sample. A possible reason why no larger crystallite sizes were observed in the sample could be related to the resolution limit of the diffraction experiment. In a scattering experiment, the observed peak broadening reflects the mean size of the crystallite size distribution in the sample. However, as crystallite size increases, the full width at half maximum (FWHM) of the diffraction peaks decreases. When the crystallite size reaches a certain threshold, the peak broadening becomes smaller than the instrumental resolution, making it impossible to resolve the larger crystallites. This limitation is likely responsible for the absence of larger crystallite sizes in the calculated data. In the AFM images, darker areas are softer or less rigid areas. These areas are easier to indent with the AFM tip and, therefore, appear darker. Crystalline regions of the material, which are stiffer, more structured and, therefore, more crystalline, may appear brighter. Thus, it can be concluded that the white spots in the AFM image (Fig. 9c) are stereocrystallites, on which PCL crystallizes as nucleation points, which is supported by the covalent linkage by of PCL to the PLLA part of the SC's. One can also see that the segments are oriented to the left-hand side.

3.6.3. Segment length quantitatively influences crystallite size and morphology. The WAXS results revealed a correlation between crystallite size of SC/HC and the PLLA block length within the multiblock copolymers (see Fig. 3). Longer PLLA segments within $P(PCL_m-b-PLLA_n)_x$ promote the formation of larger and more ordered PLA crystallites in the blends, while shorter segments restrict chain mobility, resulting in smaller and less defined crystalline domains (Fig. 10). A comparable trend is observed in the AFM phase images of $P(PCL_m-b-PLLA_n)_x$:PDLA₅₆ blends, which display distinct domain morphologies depending on the block composition. In samples with longer PLLA blocks, larger and more defined crystalline aggregates appear (bright regions), consistent with the increase in crystallite size determined from WAXS. In contrast, systems with shorter PLLA blocks exhibit smaller domain structures, whereas darker areas indicate amorphous or softer phases from PCL.

By combining AFM and TEM, direct visual evidence was obtained that supports the quantitative trends observed by WAXS. These complementary techniques confirm that the PLLA segment length quantitatively influences crystallite size and morphology, establishing a robust structure–property relationship within these materials. The hierarchical morphology observed by AFM—ranging from fine, densely packed

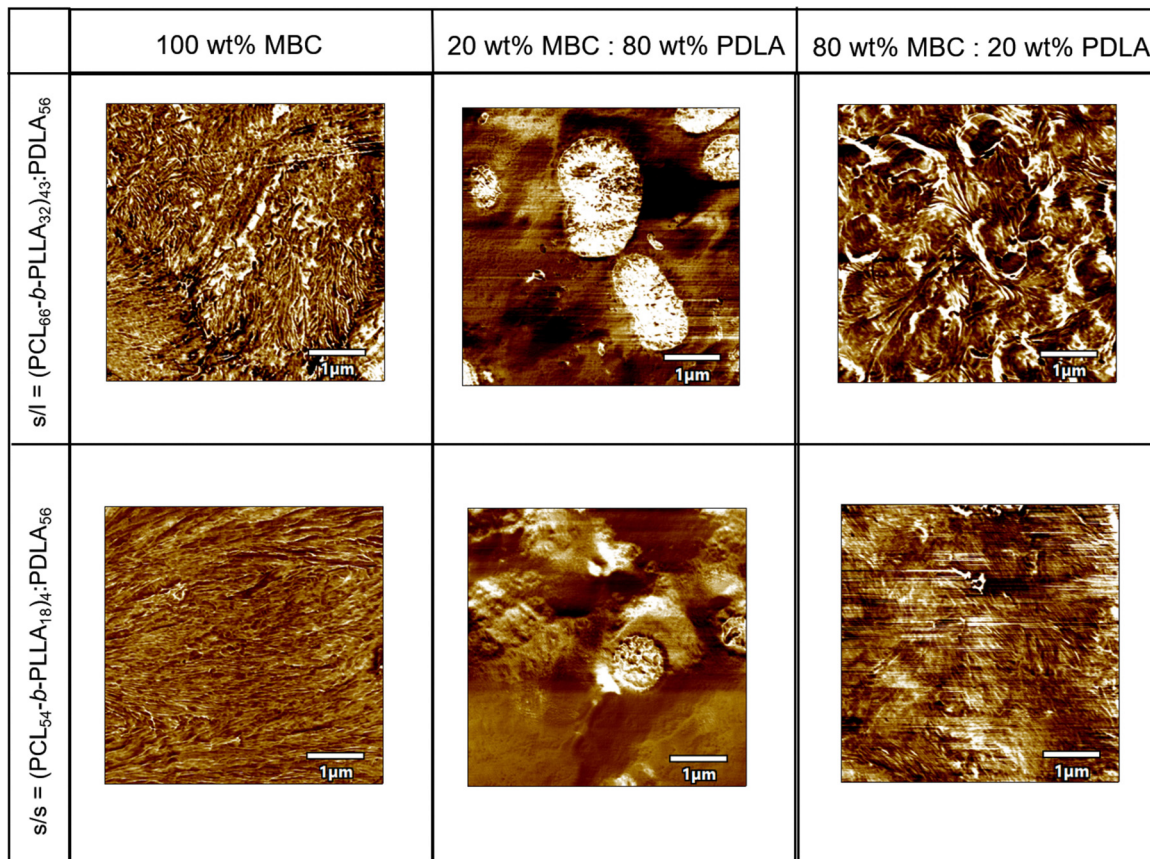


Fig. 10 AFM phase images of $\text{P}(\text{PCL}_m\text{-}b\text{-PLLA}_n)_x\text{:PDLA}_{56}$ blends showing distinct domain morphologies depending on the block composition. The bright areas correspond to stiffer, crystalline PLA domains, while darker regions represent amorphous or softer phases. In samples with longer PLLA blocks (top row), the formation of larger, more defined crystalline aggregates is observed (20 wt% MBC) and larger PLA lamella (80 wt% MBC), consistent with the increase in crystallite size determined from WAXS analysis. In contrast, shorter-block systems (bottom row) display finer phase morphology.

crystallites in short-block systems to extended lamellar aggregates in long-block systems—mirrors the crystallite size evolution determined from X-ray diffraction. Altogether, these observations confirm that the PLLA segment length quantitatively influences crystallite size and morphology, as longer blocks promote extended lamellar growth and enhanced phase separation at the nanoscale.

3.7. Mechanical properties

Some of the prepared samples exhibit inhomogeneities, *i.e.* limited mixing of MBCs and PDLA that would lead to early break along the phase boundaries. Such excessive outliers in the data were not included in the analysis. Typically, for the samples studied here, we would expect an increase of ε_b with an increase in M_w , a decrease in overall crystallinity, and an increase in the amorphous PCL phase, as this is above T_g at the temperature of measurement. Young's modulus should increase with crystallinity (though non-linearly)²⁷ and a decrease in the amorphous PCL phase. Further aspects are the different types of crystals and crystallite sizes. As shown in the POM images, a finer structure is formed with increasing MBC content. At lower MBC content spherulites are formed that may act as phase boundaries at which breakage may easily

arise and which may disturb the slip phases of the SC and PCL crystal planes. In fact, as such multiple factors play a role, all over comparison can hardly be attributed to a single structural feature. In the following, some trends within a small series of samples are discussed. The mechanical properties of the multi-block copolymers and their corresponding blends are presented in Fig. 11, 12, and Fig. S7.1, S7.2 and Table 3. It should further be noted that PLA is known to undergo stress-induced crystallization,⁸⁷ a phenomenon not studied here in detail, but which may further contribute to the observed mechanical behavior.

3.7.1. Increased ε_b with increasing PCL content and SC formation. The investigated blends possessed tensile strengths up to ~ 2.8 MPa and a high ε_b (max. $\sim 750\%$). In $\text{P}(\text{PCL}_{54}\text{-}b\text{-PLLA}_{18})_4\text{:PDLA}_{56}$ the tensile strength increased from ~ 0.3 MPa (70/30) to ~ 1.3 MPa (90/10) and the elongation at break is increased from $\sim 14\%$ to $\sim 500\%$ for the 80/20 blend. While in $\text{P}(\text{PCL}_{66}\text{-}b\text{-PLLA}_{32})_{43}\text{:PDLA}_{56}$ the tensile strength increased from ~ 1.2 MPa to ~ 1.8 MPa and the elongation at break from $\sim 340\%$ (70/30) to $\sim 514\%$ (80/20), which then decreases to $\sim 366\%$ upon further increasing the MBC content of the blend (90/10). In this series, stereocomplexes are formed in all 3 blends, but the 1:1 ratio of PDLA to PLLA is only present in



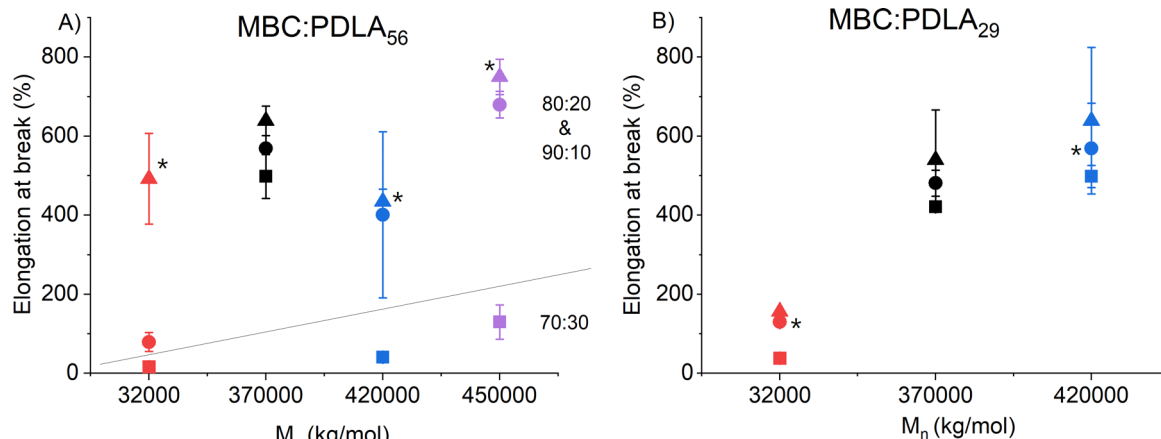


Fig. 11 Elongation at break (ε_b) as a function of molar mass (M_n) for $P(PCL_m-b-PLLA)_x:PDLa$ blends with (A) $PDLa_{56}$ and (B) $PDLa_{29}$ (■ = 70:30 MBC:PDLa, ● = 80:20, ▲ = 90:10). Each data point represents the mean value with error bars denoting the range of data. A clear M_n -dependent increase in ductility is observed for $PDLa_{29}$ blends, whereas for $PDLa_{56}$, elongation at break is primarily governed by blend composition. The 70:30 blends exhibit the lowest elongation values, while the 80:20 and 90:10 compositions, in which stereocomplex crystallites are formed, show the highest ductility.

the 80/20 mixture, which has the largest average elongation at the break. The ε_b of blends in which no SC formation occurred ($P(PCL_{113}-b-PLLA_{26})_{24}:PDLa_{29/56}$) was increasing with the MBC content with a simultaneous decrease of the Young's moduli for the $PDLa_{56}$ series ($M_n \approx 370 \text{ kg mol}^{-1}$). This went hand in hand with a slight increase in calculated M_w . The calc. M_w is basically the same for the same mixing ratios with different $PDLa$ lengths. However, there is still a trend for lower ε_b and higher Young's moduli as long as there are no SCs formed. This may indicate a stronger phase separation, while the SCs mechanically stabilize the films due to strong bonds between the phases. Such an effect is likely furthermore depending on the size of the phases, as small nanodroplets of one blend component are associated with reinforcement of the blend,

comparable to composite formation, as *e.g.* has been shown in poly(ethylene-*co*-methacrylate)/poly(vinylidene fluoride) blends.⁸⁸

In blends that formed SC at different compositions, lower absolute crystallinity would lead to lower Young's moduli and higher ε_b , as expected. The increase in the overall molar mass of the blends with $PDLa_{29}$ showed a clear influence on ε_b , indicating that molar mass plays a dominant role in governing ductility (see Fig. 11). This trend has also been reported for tri-block and di-block copolymers composed of well-defined high-molecular-weight $PDLa-b-PLLA$ and $PDLa-b-PLLA-b-PDLA$ stereoblock architectures, as shown by the group of Rastogi *et al.*⁸⁹ In their study, increasing block length and molar mass led to a pronounced enhancement in elongation at break, which was attributed to improved chain entanglement and more effective stress transfer between crystalline and amorphous domains. These observations are consistent with the present findings, where higher molar mass and optimized blend composition similarly promote ductility through enhanced phase continuity and stereocomplex-mediated reinforcement. In our case this trend can be most probably attributed to enhanced chain entanglement and improved phase continuity of the soft PCL-rich domains, allowing for greater energy dissipation during deformation.

In contrast, the $PDLa_{56}$ blends do not exhibit a straightforward correlation between M_n and elongation at break. Here, the blend composition and crystalline phase structure appear to exert a stronger influence. The 70:30 (MBC:PDLa) blends display the lowest elongation values, which likely result from a disrupted PCL phase continuity and a small fraction of brittle PLA-HC regions (see Fig. 2). Conversely, the 80:20 and 90:10 blends show the highest elongation at break, coinciding with the formation of stereocomplex (SC) crystallites. These finely dispersed SC domains act as physical cross-links that improve stress transfer and promote strain hardening without compromising flexibility. Overall, the results indicate that while molar mass primarily dictates the mechanical response in $PDLa_{29}$

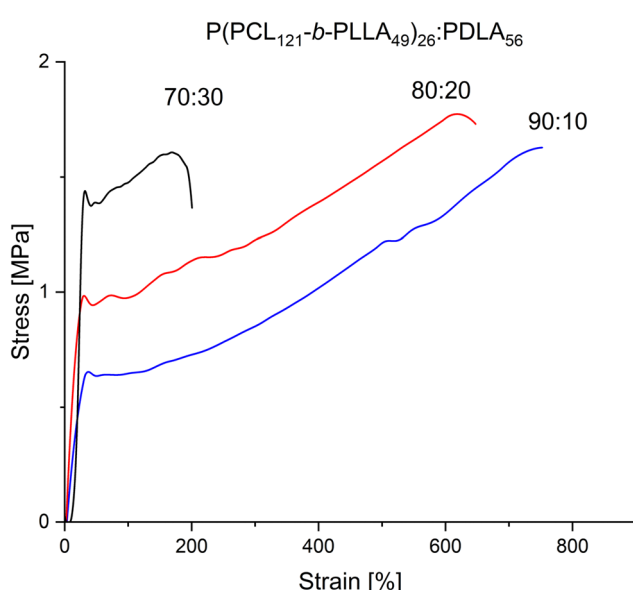


Fig. 12 Representative stress and strain curve of $P(PCL_{121}-b-PLLA_{49})_{26}:PDLa_{56}$.

Table 3 Mechanical properties of MBC:PDLA_y blends. The experiments values are reported as median values with experimental ranges (min–max) in parentheses

Material	MBC : PDLA _y	calc. M_w (kg mol ⁻¹)	Elongation at break (%)	Tensile strength at yield (MPa)	Young's modulus (kPa)
P(PCL ₅₄ - <i>b</i> -PLLA ₁₈) ₄ :PDLA ₂₉	70 : 30	37.2	38 (33–62)	0.5 (0.4–0.5)	82 (67–82)
	80 : 20	42.0	130 (128–142)	0.3 (0.3–0.3)	53 (37–57)
	90 : 10 ^b	46.8	156 (131–184)	0.5 (0.3–0.7)	35 (32–43)
P(PCL ₅₄ - <i>b</i> -PLLA ₁₈) ₄ :PDLA ₅₆	70 : 30	37.4	16 (10–18)	0.3 (0.2–0.5)	42 (38–51)
	80 : 20	42.2	492 (480–550)	1.2 (1.0–1.8)	30 (20–46)
	90 : 10 ^{ab}	46.9	79 (58–106)	0.6 (0.6–0.6)	70 (67–72)
P(PCL ₆₆ - <i>b</i> -PLLA ₃₂) ₄₃ :PDLA ₂₉	70 : 30 ^a	498	630 (580–636)	2.3 (2.3–2.5)	235 (220–280)
	80 : 20 ^{ab}	569	660 (530–760)	1.7 (1.5–1.7)	57 (43–68)
	90 : 10 ^a	639	330 (200–570)	1.3 (1.2–1.7)	86 (77–99)
P(PCL ₆₆ - <i>b</i> -PLLA ₃₂) ₄₃ :PDLA ₅₆	70 : 30 ^a	498	354 (277–389)	1.2 (1.2–1.2)	77 (75–94)
	80 : 20 ^{ab}	569	518 (442–593)	1.3 (1.1–1.7)	49 (49–76)
	90 : 10 ^a	639	305 (303–378)	1.8 (1.7–1.8)	108 (105–130)
P(PCL ₁₁₃ - <i>b</i> -PLLA ₂₆) ₂₄ :PDLA ₂₉	70 : 30	421	25 (22–38)	1.6 (1.4–1.6)	303 (230–350)
	80 : 20 ^b	481	112 (62–128)	1.7 (1.7–2.1)	312 (308–331)
	90 : 10	540	204 (48–302)	2.0 (1.7–3.4)	320 (301–380)
P(PCL ₁₁₃ - <i>b</i> -PLLA ₂₆) ₂₄ :PDLA ₅₆	70 : 30	421	41 (39–44)	1.8 (1.5–1.8)	391 (370–440)
	80 : 20 ^b	481	434 (425–488)	2.1 (2.1–2.8)	270 (217–286)
	90 : 10	540	401 (349–769)	2.4 (1.3–3.2)	151 (125–170)
P(PCL ₁₂₁ - <i>b</i> -PLLA ₄₉) ₂₆ :PDLA ₅₆	70 : 30 ^a	631	130 (113–200)	1.6 (1.2–1.9)	112 (110–130)
	80 : 20 ^{ab}	721	680 (647–714)	1.8 (1.3–2.4)	60 (48–86)
	90 : 10 ^a	810	752 (637–768)	1.0 (0.7–1.6)	22 (15–30)

^a Indicates compositions, in which SC were detected. ^b Indicates compositions, in which the PLLA : PDLA ratio is ~1 : 1.

blends, in PDLA₅₆ systems the balance between MBC : PDLA ratio and SC formation becomes the decisive factor. The combination of higher PCL phase continuity and the presence of stereocomplex crystallites enhances the ductility and mechanical resilience of the material.

3.8. Overall model

In the investigated MBCs, both blocks are principally crystallizable. While it is known that the phase separating behavior of MBCs generally can be compared to the phase separation of di- and oligoblock copolymers (“effective diblock copolymer model”⁹⁰), the restricted freedom of movement in MBC typically reduces the crystallizability, *i.e.* longer sequences are required for crystal formation than in homopolymers or diblock copolymers. In the studied system, a further facet is the ratio between PCL and PLLA block, simultaneously leading to a change in wt% content. While increasing the PCL content leads to “dilution” of PLA, and this effect certainly plays a role, the absolute segment length is a different kind of factor, assuming a PCL/PLLA interphase between the PCL and PLLA domains. This interphase reduces the segment length available for crystallization, and while the segment length seems to be sufficient for PLA crystallization in the studied s/s, s/l, and l/l MBCs (Fig. 12A), no PLLA crystallization is possible in l/s MBCs (Fig. 13B).

In the present study, the long/short multiblock copolymer (l/s MBC) is composed of P(PCL₁₁₃-*b*-PLLA₂₆)₂₄ blended with PDLA₂₉. In contrast, the MBC investigated by Jikei *et al.*, consisting of PLLA₂₂-*b*-PCL₄₉ mixed with PDLA₂₇, demonstrated stereocomplex (SC) formation at a 1 : 1 molar ratio.²⁵ Both systems exhibit a comparable PCL-to-PLLA block length ratio of

approximately 2 : 1. However, SC formation was only observed in our work in the system with shorter PCL chains (PCL₄₉), whereas no stereocomplexation occurred in the system containing longer PCL chains (PCL₁₁₃), despite the equimolar mixing of the complementary PLLA/PDLA segments. Consequently, the ability to form stereocomplex crystallites is no longer governed solely by the PLA enantiomer ratio but becomes increasingly dependent on the PCL block length and is able to hinder even PLA HC crystallization. This phenomenon could also be shown to some extend in other blends were the comonomer is miscible in the melt or solvent phase *e.g.* in PLA₂₀-*b*-PBS₈₀ MBCs, although the number of repeating units to inhibit SC formation completely are considerably higher compared to PCL.⁹¹

This interpretation is supported by the fact that blends of l/s MBCs with overall higher wt% PLA content do not crystallize compared to other MBCs with altogether lower PLA content. Compared to PLA homopolymer mixtures which are able to form homocrystallites regardless of their molar mass or chain length shown in blends with a molar mass of >200 kg mol⁻¹.⁹²

Furthermore, small domain sizes correlate with a relatively larger content of interphases. When forming blends with larger amounts of PDLA, the observed HCs can be attributed to PDLA homocrystallization alone, while crystallization of PLLA and PCL is inhibited (Fig. 13C). At higher MBC content, SC formation is observed, most likely occurring through wrapping of the PLLA segments around PDLA (Fig. 13D), though HC formation may also occur, again putatively to be attributed to the PDLA phase. It must be noted that also the molar mass of the PDLA component had a major impact on the overall crystallization process, with a crystallization tendency of PDLA₂₉ > PDLA₁₅ > PDLA₅₆.



Polymer film formation by slow solvent evaporation from the blend solution is another factor and has been employed here, which is associated with shifting a presumed equilibrium between SC and HC formation towards HCs.⁹⁰ Films offer defined two-dimensional geometries, facilitate surface-sensitive analyses, and are widely used in biomedical applications such as coatings, membranes, or drug delivery systems.^{7,30}

Specifically, the formation of SCs requires intermolecular interactions between enantiomeric PLLA and PDLA chains prior to crystallization. A key aspect is the establishment of hydrogen bonds between opposing ester groups of the helical chains. For this interaction to occur, the crystallization kinetics must be carefully balanced – sufficiently slow to allow enantiomeric chain alignment, but not so prolonged that phase separation dominates, particularly in PDLA-rich blends. This balance is particularly critical when working with copolymers, where chain mobility, block architecture, and molecular weight significantly influence the accessibility and compatibility of the stereoregular sequences. Therefore, a delicate balance between kinetic control and miscibility is essential to enable effective SC formation. In multiblock systems, this equilibrium is further modulated by PCL-induced chain mobility and block length constraints.

The crystallization of HC homocrystallites is especially prevalent in high molar mass blends where the formation of a uniform film is not possible under certain conditions, and in consequence, the SC formation is hindered.¹⁷ This has likely happened in our study as well, as in some samples SC and HCs are present and the SC content in these samples could be increased by annealing. However, annealing led only to higher SC content in samples that already contained some SCs.

Consistent with the data from AFM, POM and TEM is the understanding that in the film formation process first PLA crystallization occurs, followed by PCL crystallization. This would be expected in any case for crystallization from the melt, but seems also to be applicable for slow solvent evaporation. The size of PLA HC spherulites and SC star-like structures is, hence, dependent on the overall composition of the blend and crystallite sizes correlate with segment length, while PCL then must accommodate itself within the formed structure. This occurs by partial crystallization, with the PLA SCs acting as nucleation points, as in blends with only HC of PDLA the formed PCL domains mainly remain amorphous.

Blends that enable SC formation and show fine distribution of small crystallites in a semicrystalline matrix of overall low crystallinity could be demonstrated to have excellent ε_b values

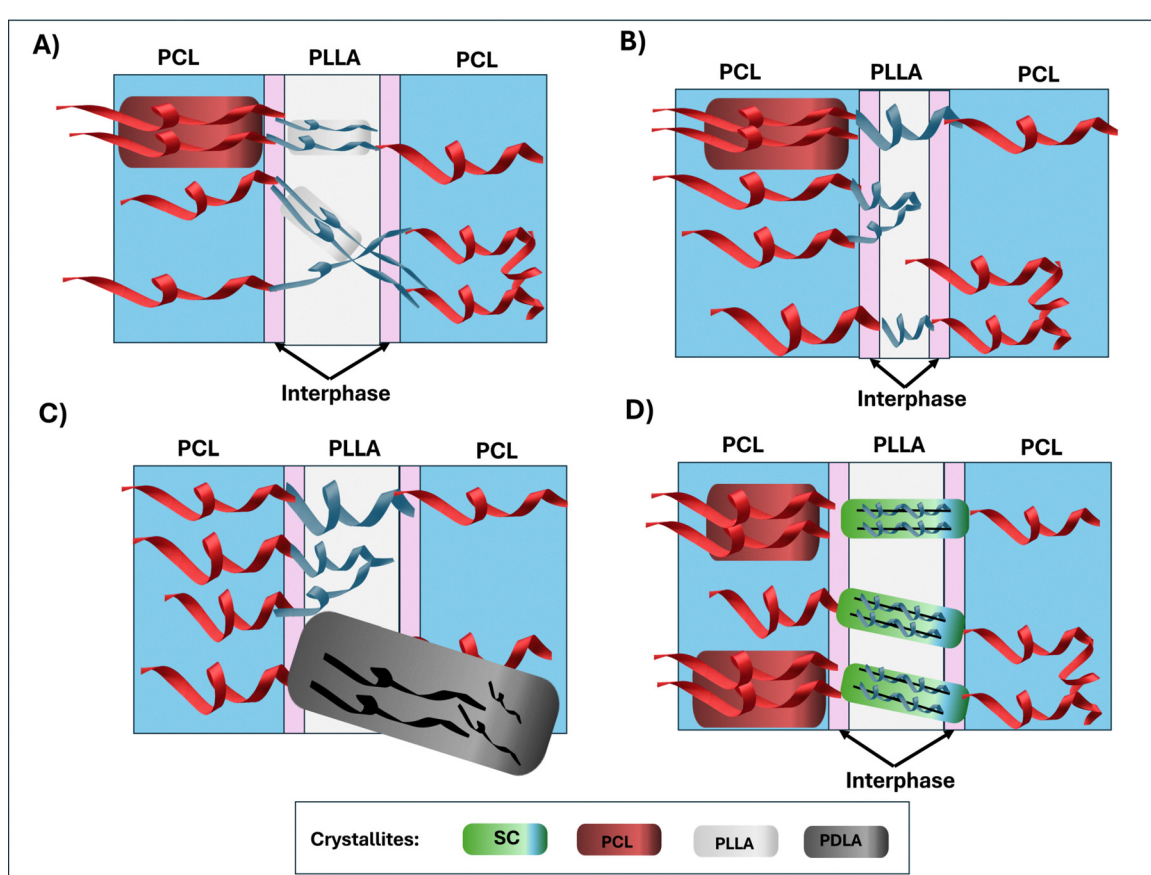


Fig. 13 Visualizing overall phase organization conditions (A) PCL and PLLA both crystallizable, with small interphase. (B) In l/s MBC, the PLLA domains may be so small that no HC formation is possible. (C) In blends with large amounts of PDLA, PDLA homocrystallization is predominant. (D) In blends with larger MBC content where SC formation is possible, PLLA segments wrap around the shorter PDLA chains, and the SC's act as nucleation points for PCL crystallization.

up to 752%, highlighting the effect of crystallite size, distribution and crystallinity on the mechanical properties. Altogether, the mechanical properties reflect the complex interplay between confinement of crystallization, plasticization through the PCL phase, and the effect of nucleation points.

4. Conclusions

In this study, casted films of multiblock copolymers of $P(PCL_m-b-PLLA_n)_x$ and their blends with PDLA_y with different molar masses were prepared and the thermal transitions, mechanical properties and phase morphology were investigated. By characterizing and linking data from multiple techniques and analyzing them over different length scales, we could better understand the factors that influence the phase morphology of $P(PCL_m-b-PLLA_n)_x$:PDLA_y and, therefore, understand the relationship between structure and properties. This holistic approach shall enable more precise tuning of material properties for specific applications. Although previous studies examined stereocomplex formation and mechanical properties in $P(PCL-b-PLLA)$ -MBCs, the systematic effect of block lengths, block ratios, and PDLA chain length on the formation and stabilization of stereocomplex phases in $P(PCL_m-b-PLLA_n)_x$:PDLA_y systems has not yet been fully understood.^{25,26} We systematically correlated block lengths with crystallite sizes and crystallinity. For instance, SC crystallites (5–13 nm) and PCL crystallites (1–20 nm) vary with PCL/PLLA ratios, a level of granularity absent in studies using PEG or PLGA. WAXS showed SC formation in 1:1 up to 1:4 blends (PLLA:PDLA). SC formation is favored over PLA HC formation, and SC's act as nucleation points for the crystallization of PCL.

The minimum block length of PLLA in the MBCs is only one aspect to allow SC formation. The SC formation can be suppressed, when PLLA blocks at the lower sequence length for allowing SC formation (~15–25 units) are coupled to much longer PCL segments; this is putatively linked to a PCL/PLLA interphase that effectively reduces the segment length of PLLA available for crystallization. Crystallite sizes vary with the composition between 1–8 nm (SC), 1–20 nm (PCL) and 1–50 nm (HC), and there was a trend for an increase of crystallite size with sequence length. Relative crystallinities of 6–70% (SC), 2–80% (PCL) and 3–80% (HC) were achieved. A uniform distribution of stereocomplexes within the polymer matrix was confirmed by TEM, AFM and POM. A diverse crystal morphology and superstructure, characterized by well-defined Maltese-cross spherulites of HC and the formation of short and long shish-kebab-like SC crystals surrounded by a semicrystalline PCL matrix were observed. Of note is that while the phase separation in the blends somewhat hindered crystallization, the formation of one type of crystal, especially SCs, was revealed to act as a nucleation point for also other crystal types, which likely was supported through the covalent linkage of PCL and PLLA blocks.

Our findings for the solution casted films reveal morphologies similar to those formed through melt processing, highlighting comparable structural features despite differing

fabrication methods. This suggests a sequential crystallization process, starting with the crystallization of SCs, then HCs, and finally PCL, similar to processes observed in crystallization from the melt. The presented data and overall model shall in the future be used to tailor block lengths in the MBC and PDLA part to design blends with specific phase structure and properties, which is of interest *e.g.* for biological applications.²⁷ Such material design can likely be supported through the use of computer models.^{93,94} The novelty of the present work lies in the introduction of a dual approach combining precise multiblock copolymer design with systematic compositional blending to study stereocomplex formation in PLA-based materials. Previous studies have primarily relied on physically mixed PLLA/PDLA systems or simpler di- and triblock copolymers, where phase separation and limited molecular control obscure the intrinsic effects of block sequence and composition. In contrast, the multiblock copolymers $P(PCL_m-b-PLLA_n)$ synthesized here provide molecular precision and covalent connectivity between soft (PCL) and hard (PLLA) segments, enabling controlled crystallization behavior. By blending with PDLA from 90:10 to 20:80, we map the evolution from HC-dominated to SC-dominated states and correlate architecture and composition with crystallinity, melting behavior, and lamellar organization/morphology. This correlative approach allows for a mechanistic understanding of how molecular architecture and blend composition govern phase formation. Moreover, the underlying synthetic strategy can be readily adapted to other aliphatic polyester systems (*e.g.*, PEG-PLA, PHB-PLA), providing a general platform for tailoring hierarchical structures in semicrystalline biodegradable materials.

Author contributions

Conceptualization: Armando J. Mandlule, Axel T. Neffe; methodology: Armando J. Mandlule, Axel T. Neffe, Berit Zeller-Plumhoff, D. C. Florian Wieland; formal analysis and investigation: Armando J. Mandlule, Yue Liu, Susanne Schwanz, Yvonne Pieper, Heike Scharf, D. C. Florian Wieland, Berit Zeller-Plumhoff, André Conceicao, Iskhakova Kamila, Axel T. Neffe; writing – original draft preparation: Armando J. Mandlule, Axel T. Neffe; writing – review and editing: Armando J. Mandlule, Axel T. Neffe; Yue Liu, Susanne Schwanz, Yvonne Pieper, Heike Scharf, D. C. Florian Wieland, Berit Zeller-Plumhoff, André Conceicao, Francesca M. Toma; resources: Francesca M. Toma, Axel T. Neffe; supervision: Axel T. Neffe.

Conflicts of interest

The authors declare no competing interests or conflicts of interest.

Data availability

Data for this publication, including raw and processed data from differential scanning calorimetry (DSC), tensile testing,



wide-angle X-ray scattering (WAXS), transmission electron microscopy (TEM), atomic force microscopy (AFM), polarized optical microscopy (POM), gel permeation chromatography (GPC), and nuclear magnetic resonance spectroscopy (NMR) and the corresponding metadata, are available at Figshare, DOI: <https://doi.org/10.6084/m9.figshare.29825372>. The dataset includes original instrument output files in different formats. Several experimental descriptions and additional figures and tables have been included as supplementary information (SI). See DOI: <https://doi.org/10.1039/d5ma00886g>.

Acknowledgements

This work was funded by the Helmholtz Association and the Joint Lab “Model and Data-driven Materials Characterization” (MDMC), a cross-centre platform of the Helmholtz Association. We acknowledge DESY (Hamburg, Germany), a member of the Helmholtz Association HGF, for the provision of experimental facilities. Parts of this research were carried out at PETRA III and we would like to thank SAXSMAT beamline staff for assistance. Beamtime was allocated for proposal 20231350.

References

1. J. Rydz, W. Sikorska, M. Kyulavska and D. Christova, Polyester-based (bio) degradable polymers as environmentally friendly materials for sustainable development, *Int. J. Mol. Sci.*, 2014, **16**(1), 564–596.
2. B. L. Cunha, J. O. Bahú, L. F. Xavier, S. Crivellin, S. D. de Souza, L. Lodi, A. L. Jardini, R. M. Filho, M. I. Schiavon and V. O. C. Concha, Lactide: production routes, properties, and applications, *Bioengineering*, 2022, **9**(4), 164.
3. M. Hofmann, C. Alberti, F. Scheliga, R. R. Meißner and S. Enthaler, Tin(II) 2-ethylhexanoate catalysed methanolysis of end-of-life poly(lactide), *Polym. Chem.*, 2020, **11**(15), 2625–2629.
4. H. Ramaraju, R. E. Akman, D. L. Safranski and S. J. Hollister, Designing biodegradable shape memory polymers for tissue repair, *Adv. Funct. Mater.*, 2020, **30**(44), 2002014.
5. S. Dai, Z. Dai, N. Jiang, Z. Ning and Z. Gan, Highly toughened poly(L-lactide) by poly(D-lactide)-containing crosslinked polyurethane shows excellent malleability, flexibility and shape memory property, *Polymer*, 2022, **262**, 125482.
6. M. A. Hillmyer and W. B. Tolman, Aliphatic polyester block polymers: renewable, degradable, and sustainable, *Acc. Chem. Res.*, 2014, **47**(8), 2390–2396.
7. H. Seyednejad, A. H. Ghassemi, C. F. van Nostrum, T. Vermonden and W. E. Hennink, Functional aliphatic polyesters for biomedical and pharmaceutical applications, *J. Controlled Release*, 2011, **152**(1), 168–176.
8. H. Tsuji, Poly(lactide) stereocomplexes: formation, structure, properties, degradation, and applications, *Macromol. Biosci.*, 2005, **5**(7), 569–597.
9. X. Zhao, H. Hu, X. Wang, X. Yu, W. Zhou and S. Peng, Super tough poly(lactic acid) blends: a comprehensive review, *RSC Adv.*, 2020, **10**(22), 13316–13368.
10. X. Zhou, J. Deng, C. Fang, W. Lei, Y. Song, Z. Zhang, Z. Huang and Y. Li, Additive manufacturing of CNTs/PLA composites and the correlation between microstructure and functional properties, *J. Mater. Sci. Technol.*, 2021, **60**, 27–34.
11. H. Tsuji and Y. Tezuka, Stereocomplex formation between enantiomeric poly(lactic acid)s. 12. Spherulite growth of low-molecular-weight poly(lactic acid)s from the melt, *Biomacromolecules*, 2004, **5**(4), 1181–1186.
12. Y. Fan, H. Nishida, Y. Shirai, Y. Tokiwa and T. Endo, Thermal degradation behaviour of poly(lactic acid) stereocomplex, *Polym. Degrad. Stab.*, 2004, **86**(2), 197–208.
13. D. Brizzolara, H.-J. Cantow, K. Diederichs, E. Keller and A. J. Domb, Mechanism of the stereocomplex formation between enantiomeric poly(lactide)s, *Macromolecules*, 1996, **29**(1), 191–197.
14. M. Jikei, Y. Takeyama, Y. Yamamoto, N. Shinbo, K. Matsumoto, M. Motokawa, K. Ishibashi and F. Yamamoto, Synthesis and properties of Poly(L-lactide)-Poly(ε-caprolactone) multiblock copolymers by the self-polycondensation of diblock macromonomers, *Polym. J.*, 2015, **47**(10), 657–665.
15. H. Younes and D. Cohn, Morphological study of biodegradable PEO/PLA block copolymers, *J. Biomed. Mater. Res.*, 1987, **21**(11), 1301–1316.
16. D. Cohn and A. H. Salomon, Designing biodegradable multiblock PCL/PLA thermoplastic elastomers, *Biomaterials*, 2005, **26**(15), 2297–2305.
17. R. M. Michell, V. Ladelta, E. Da Silva, A. J. Müller and N. Hadjichristidis, Poly(lactic acid) stereocomplexes based molecular architectures: Synthesis and crystallization, *Prog. Polym. Sci.*, 2023, **146**, 101742.
18. J. M. Schultz, Microstructural aspects of failure in semicrystalline polymers, *Polym. Eng. Sci.*, 1984, **24**(10), 770–785.
19. Dijk-Wolthuis, J. Kettenes-Van Den Bosch, P. Schuyl and W. Hennink, Monodisperse enantiomeric lactic acid oligomers: Preparation, characterization, and stereocomplex formation, *Macromolecules*, 1998, **31**(19), 6397–6402.
20. L. Peponi, I. Navarro-Baena, J. E. Báez, J. M. Kenny and A. Marcos-Fernández, Effect of the molecular weight on the crystallinity of PCL-*b*-PLLA di-block copolymers, *Polymer*, 2012, **53**(21), 4561–4568.
21. R. J. Spontak and S. D. Smith, Perfectly-alternating linear (AB)_n multiblock copolymers: Effect of molecular design on morphology and properties, *J. Polym. Sci., Part B: Polym. Phys.*, 2001, **39**(9), 947–955.
22. G. P. Baeza, Recent advances on the structure–properties relationship of multiblock copolymers, *J. Polym. Sci.*, 2021, **59**(21), 2405–2433.
23. N. J. Rebello, A. Arora, H. Mochigase, T.-S. Lin, J. Shi, D. J. Audus, E. S. Muckley, A. Osmani and B. D. Olsen, The Block Copolymer Phase Behavior Database, *J. Chem. Inf. Model.*, 2024, **64**(16), 6464–6476.
24. Z. Jing, X. Shi, G. Zhang and J. Gu, Synthesis and properties of poly(lactide)/poly(ε-caprolactone) multiblock

supramolecular polymers bonded by the self-complementary quadruple hydrogen bonding, *Polymer*, 2017, **121**, 124–136.

25 M. Jikei, T. Suga, Y. Yamamoto and K. Matsumoto, Synthesis and properties of poly(L-lactide-*co*-glycolide)-*b*-Poly(ϵ -caprolactone) multiblock copolymers formed by self-polycondensation of diblock macromonomers, *Polym. J.*, 2017, **49**(4), 369–375.

26 V. Izraylit, O. E. Gould, T. Rudolph, K. Kratz and A. Lendlein, Controlling actuation performance in physically cross-linked polylactone blends using polylactide stereocomplexation, *Biomacromolecules*, 2019, **21**(2), 338–348.

27 A. T. Neffe, V. Izraylit, P. J. Hommes-Schattmann and A. Lendlein, Soft, Formstable (Co) Polyester Blend Elastomers, *Nanomaterials*, 2021, **11**(6), 1472.

28 T. Suga, N. T. Xuyen, K. Matsumoto, M. Jikei, K. Takahashi, H. Kubota and T. Tamura, Enhanced proliferation of HeLa cells on PLLA-PCL and PLGA-PCL multiblock copolymers, *Polym. J.*, 2017, **49**(7), 567–573.

29 Z. Jing, X. Huang, X. Liu, M. Liao, Z. Zhang and Y. Li, Crystallization, thermal and mechanical properties of stereocomplexed poly(lactide) with flexible PLLA/PCL multiblock copolymer, *RSC Adv.*, 2022, **12**(21), 13180–13191.

30 J. Fernández, A. Larrañaga, A. Etxeberria, W. Wang and J. Sarasua, A new generation of poly(lactide- ϵ -caprolactone) polymeric biomaterials for application in the medical field, *J. Biomed. Mater. Res., Part A*, 2014, **102**(10), 3573–3584.

31 U. Ojha, P. Kulkarni, J. Singh and R. Faust, Syntheses, characterization, and properties of multiblock copolymers consisting of polyisobutylene and poly(L-lactide) segments, *J. Polym. Sci., Part A: Polym. Chem.*, 2009, **47**(14), 3490–3505.

32 A. Takagi, Y.-I. Hsu and H. Uyama, Biodegradable poly(lactic acid) and polycaprolactone alternating multiblock copolymers with controllable mechanical properties, *Polym. Degrad. Stab.*, 2023, **218**, 110564.

33 J. S. Moore and S. I. Stupp, Room temperature polyesterification, *Macromolecules*, 1990, **23**(1), 65–70.

34 S. Barcza, Molecular Weight Determination by Nmr Spectroscopy, *J. Org. Chem.*, 1963, **28**(7), 1914–1915.

35 V. Crescenzi, G. Manzini, G. Calzolari and C. Borri, Thermodynamics of fusion of poly- β -propiolactone and poly- ϵ -caprolactone. comparative analysis of the melting of aliphatic polylactone and polyester chains, *Eur. Polym. J.*, 1972, **8**(3), 449–463.

36 Z. Liu, M. Fu, F. Ling, G. Sui, H. Bai, Q. Zhang and Q. Fu, Stereocomplex-type polylactide with bimodal melting temperature distribution: toward desirable melt-processability and thermomechanical performance, *Polymer*, 2019, **169**, 21–28.

37 H.-S. Park and C.-K. Hong, Relationship between the Stereocomplex Crystallization Behavior and Mechanical Properties of PLLA/PDLA Blends, *Polymers*, 2021, **13**(11), 1851.

38 S. Haas, X. Sun, A. Conceição, J. Horbach and S. Pfeffer, The new small-angle X-ray scattering beamline for materials research at PETRA III: SAXSMAT beamline P62, *J. Synchrotron Radiat.*, 2023, **30**(6), 1156–1167.

39 U. Holzwarth and N. Gibson, The Scherrer equation versus the 'Debye–Scherrer equation', *Nat. Nanotechnol.*, 2011, **6**(9), 534.

40 H. K. Nguyen, M. Ito and K. Nakajima, Elastic and viscoelastic characterization of inhomogeneous polymers by bimodal atomic force microscopy, *Jpn. J. Appl. Phys.*, 2016, **55**(8S1), 08NB06.

41 P. Pan, L. Han, J. Bao, Q. Xie, G. Shan and Y. Bao, Competitive stereocomplexation, homocrystallization, and polymorphic crystalline transition in poly(L-lactic acid)/poly(D-lactic acid) racemic blends: molecular weight effects, *J. Phys. Chem. B*, 2015, **119**(21), 6462–6470.

42 L. Aliotta, P. Cinelli, M. B. Coltell, M. C. Righetti, M. Gazzano and A. Lazzeri, Effect of nucleating agents on crystallinity and properties of poly(lactic acid)(PLA), *Eur. Polym. J.*, 2017, **93**, 822–832.

43 N. Patil, T. Narayanan, L. Michels, E. T. B. Skjønsfjell, M. Guizar-Sicairos, N. Van den Brande, R. Claessens, B. Van Mele and D. W. Breiby, Probing Organic Thin Films by Coherent X-ray Imaging and X-ray Scattering, *ACS Appl. Polym. Mater.*, 2019, **1**(7), 1787–1797.

44 Y.-T. Hsieh, S. Nozaki, M. Kido, K. Kamitani, K. Kojio and A. Takahara, Crystal polymorphism of polylactide and its composites by X-ray diffraction study, *Polym. J.*, 2020, **52**(7), 755–763.

45 Y. Yin, G. Liu, Y. Song, X. Zhang, S. de Vos, R. Wang, C. A. Joziasse and D. Wang, Formation of stereocomplex in enantiomeric poly(lactide)s via recrystallization of homocrystals: An in situ X-ray scattering study, *Eur. Polym. J.*, 2016, **82**, 46–56.

46 S. Jiang, X. Ji, L. An and B. Jiang, Crystallization behavior of PCL in hybrid confined environment, *Polymer*, 2001, **42**(8), 3901–3907.

47 I. Navarro-Baena, A. Marcos-Fernandez, J. M. Kenny and L. Peponi, Crystallization behavior of diblock copolymers based on PCL and PLLA biopolymers, *J. Appl. Crystallogr.*, 2014, **47**(6), 1948–1957.

48 X. Wang, H. Zhao, L.-S. Turng and Q. Li, Crystalline Morphology of Electrospun Poly(ϵ -caprolactone) (PCL) Nanofibers, *Ind. Eng. Chem. Res.*, 2013, **52**(13), 4939–4949.

49 S. Hassanzadeh-Tabrizi, Precise calculation of crystallite size of nanomaterials: a review, *J. Alloys Compd.*, 2023, **968**, 171914.

50 Y. Ikada, K. Jamshidi, H. Tsuji and S. H. Hyon, Stereocomplex formation between enantiomeric poly(lactides), *Macromolecules*, 1987, **20**(4), 904–906.

51 K. Tashiro, N. Kouno, H. Wang and H. Tsuji, Crystal structure of poly(lactic acid) stereocomplex: random packing model of PDLA and PLLA chains as studied by X-ray diffraction analysis, *Macromolecules*, 2017, **50**(20), 8048–8065.

52 H. Tsuji and Y. Ikada, Stereocomplex formation between enantiomeric poly(lactic acid)s. XI. Mechanical properties and morphology of solution-cast films, *Polymer*, 1999, **40**(24), 6699–6708.

53 K. Shi, G. Liu, H. Sun, B. Yang and Y. Weng, Effect of biomass as nucleating agents on crystallization behavior of polylactic acid, *Polymers*, 2022, **14**(20), 4305.



54 M. Cocca, M. L. Di Lorenzo, M. Malinconico and V. Frezza, Influence of crystal polymorphism on mechanical and barrier properties of poly(L-lactic acid), *Eur. Polym. J.*, 2011, **47**(5), 1073–1080.

55 M. L. Di Lorenzo, P. Rubino, B. Immirzi, R. Luijkx, M. Hélou and R. Androsch, Influence of chain structure on crystal polymorphism of poly(lactic acid). Part 2. Effect of molecular mass on the crystal growth rate and semicrystalline morphology, *Colloid Polym. Sci.*, 2015, **293**, 2459–2467.

56 J. Puiggali, Y. Ikada, H. Tsuji, L. Cartier, T. Okihara and B. Lotz, The frustrated structure of poly(L-lactide), *Polymer*, 2000, **41**(25), 8921–8930.

57 I. Castilla-Cortázar, A. Vidaurre, B. Mari and A. J. Campillo-Fernández, Morphology, crystallinity, and molecular weight of poly(ϵ -caprolactone)/graphene oxide hybrids, *Polymers*, 2019, **11**(7), 1099.

58 A. Keller, A note on single crystals in polymers: evidence for a folded chain configuration, *Philos. Mag.*, 1957, **2**(21), 1171–1175.

59 R. Dell'Erba, G. Groeninckx, G. Maglio, M. Malinconico and A. Migliozzi, Immiscible polymer blends of semicrystalline biocompatible components: thermal properties and phase morphology analysis of PLLA/PCL blends, *Polymer*, 2001, **42**(18), 7831–7840.

60 C. Zhou, H. Li, W. Zhang, J. Li, S. Huang, Y. Meng, J. D. Christiansen, D. Yu, Z. Wu and S. Jiang, Direct investigations on strain-induced cold crystallization behavior and structure evolutions in amorphous poly(lactic acid) with SAXS and WAXS measurements, *Polymer*, 2016, **90**, 111–121.

61 K. Das, D. Ray, I. Banerjee, N. Bandyopadhyay, S. Sengupta, A. K. Mohanty and M. Misra, Crystalline morphology of PLA/clay nanocomposite films and its correlation with other properties, *J. Appl. Polym. Sci.*, 2010, **118**(1), 143–151.

62 R. H. Boyd, Relaxation processes in crystalline polymers: experimental behaviour—a review, *Polymer*, 1985, **26**(3), 323–347.

63 K. Saalwächter, T. Thurn-Albrecht and W. Paul, Recent progress in understanding polymer crystallization, *Macromol. Chem. Phys.*, 2023, **224**(7), 2200424.

64 R. Kurz, M. Schulz, F. Scheliga, Y. Men, A. Seidlitz, T. Thurn-Albrecht and K. Saalwächter, Interplay between crystallization and entanglements in the amorphous phase of the crystal-fixed polymer poly(ϵ -caprolactone), *Macromolecules*, 2018, **51**(15), 5831–5841.

65 J.-L. Wang and C.-M. Dong, Physical properties, crystallization kinetics, and spherulitic growth of well-defined poly(ϵ -caprolactone)s with different arms, *Polymer*, 2006, **47**(9), 3218–3228.

66 J.-C. Jeong, J. Lee and K. Cho, Effects of crystalline microstructure on drug release behavior of poly(ϵ -caprolactone) microspheres, *J. Controlled Release*, 2003, **92**(3), 249–258.

67 Y. Xu, Y. Xiong and S. Guo, Effect of liquid plasticizers on crystallization of PCL in soft PVC/PCL/plasticizer blends, *J. Appl. Polym. Sci.*, 2020, **137**(24), 48803.

68 A. Fernández-Tena, R. A. Pérez-Camargo, O. Coulembier, L. Sangroniz, N. Aranburu, G. Guerrica-Echevarria, G. Liu, D. Wang, D. Cavallo and A. J. Müller, Effect of Molecular Weight on the Crystallization and Melt Memory of Poly(ϵ -caprolactone)(PCL), *Macromolecules*, 2023, **56**(12), 4602–4620.

69 H. Tsuji and L. Bouapao, Stereocomplex formation between poly(L-lactic acid) and poly(D-lactic acid) with disproportionately low and high molecular weights from the melt, *Polym. Int.*, 2012, **61**(3), 442–450.

70 M. L. Di Lorenzo, Calorimetric analysis of the multiple melting behavior of poly(L-lactic acid), *J. Appl. Polym. Sci.*, 2006, **100**(4), 3145–3151.

71 R. Liao, B. Yang, W. Yu and C. Zhou, Isothermal cold crystallization kinetics of polylactide/nucleating agents, *J. Appl. Polym. Sci.*, 2007, **104**(1), 310–317.

72 J. Shao, S. Xiang, X. Bian, J. Sun, G. Li and X. Chen, Remarkable melting behavior of PLA stereocomplex in linear PLLA/PDLA blends, *Ind. Eng. Chem. Res.*, 2015, **54**(7), 2246–2253.

73 Z. Xiong, G. Liu, X. Zhang, T. Wen, S. de Vos, C. Joziasse and D. Wang, Temperature dependence of crystalline transition of highly-oriented poly(L-lactide)/poly(D-lactide) blend: In-situ synchrotron X-ray scattering study, *Polymer*, 2013, **54**(2), 964–971.

74 H. Tsuji, M. Yamasaki and Y. Arakawa, Synthesis and Stereocomplexation of New Enantiomeric Stereo Periodical Copolymers Poly(L-lactic acid-L-lactic acid-D-lactic acid) and Poly(D-lactic acid-D-lactic acid-L-lactic acid), *Macromolecules*, 2021, **54**(13), 6226–6237.

75 C. Sun, Y. Zheng, S. Xu, L. Ni, X. Li, G. Shan, Y. Bao and P. Pan, Role of Chain Entanglements in the Stereocomplex Crystallization between Poly(lactic acid) Enantiomers, *ACS Macro Lett.*, 2021, **10**(8), 1023–1028.

76 J. Liu, X. Qi, Q. Feng and Q. Lan, Suppression of Phase Separation for Exclusive Stereocomplex Crystallization of a High-Molecular-Weight Racemic Poly(L-lactide)/Poly(D-lactide) Blend from the Glassy State, *Macromolecules*, 2020, **53**(9), 3493–3503.

77 J. Anakabe, A. M. Zaldua Huici, A. Eceiza, A. Arbelaitz and L. Avérous, Combined effect of nucleating agent and plasticizer on the crystallization behaviour of polylactide, *Polym. Bull.*, 2017, **74**(12), 4857–4886.

78 X. Wang, J. Mi, J. Wang, H. Zhou and X. Wang, Multiple actions of poly(ethylene octene) grafted with glycidyl methacrylate on the performance of poly(lactic acid), *RSC Adv.*, 2018, **8**(60), 34418–34427.

79 K. Watanabe and J. Kumaki, Extended-chain crystallization and stereocomplex formation of polylactides in a Langmuir monolayer, *Polym. J.*, 2020, **52**(6), 601–613.

80 E. M. Woo and L. Chang, Crystallization and morphology of stereocomplexes in nonequimolar mixtures of poly(L-lactic acid) with excess poly(D-lactic acid), *Polymer*, 2011, **52**(26), 6080–6089.

81 Y. Xie, W. Yu, T. Xia, R. K. O'Reilly and A. P. Dove, Stereocomplex-Driven Morphological Transition of Coil-Rod-Coil Poly(lactic acid)-Based Cylindrical Nanoparticles, *Macromolecules*, 2023, **56**(19), 7689–7697.

82 S. Saeidlou, M. A. Huneault, H. Li, P. Sammut and C. B. Park, Evidence of a dual network/spherulitic crystalline morphology in PLA stereocomplexes, *Polymer*, 2012, **53**(25), 5816–5824.

83 T. Chou, P. Prayoonthong, A. Aitouchen and M. Libera, Nanoscale artifacts in RuO₄-stained poly(styrene), *Polymer*, 2002, **43**(7), 2085–2088.

84 M. Shahnooshi, K. Schneider, A. Javadi and V. Altstädt, Reprocessible nanohybrid shish-kebab superstructures of poly(lactic acid) crystallites evolving in quiescent melt: soft epitaxy nucleation in correlation with mechanics, *Polymer*, 2023, **283**, 126254.

85 V. H. Mareau and R. E. Prud'Homme, In-situ hot stage atomic force microscopy study of poly(ϵ -caprolactone) crystal growth in ultrathin films, *Macromolecules*, 2005, **38**(2), 398–408.

86 G. Molinari, P. Parlanti, L. Aliotta, A. Lazzeri and M. Gemmi, TEM morphological analysis of biopolymers: The case of Poly(Lactic Acid)(PLA), *Mater. Today Commun.*, 2024, **38**, 107868.

87 A. Vozniak and Z. Bartczak, Deformation of Poly-L-lactid acid (PLLA) under Uniaxial Tension and Plane-Strain Compression, *Polymers*, 2021, **13**(24), 4432.

88 S. Remanan, S. Ghosh, T. K. Das and N. C. Das, Nano to microblend formation in poly(ethylene-*co*-methyl acrylate)/poly(vinylidene fluoride) blend and investigation of its anomalies in rheological properties, *Nano-Struct. Nano-Objects*, 2020, **23**, 100487.

89 F. Li, F. Zhou, D. Romano and S. Rastogi, Synthesis and characterization of well-defined high-molecular-weight PDLA-*b*-PLLA and PDLA-*b*-PLLA-*b*-PDLA stereo-block copolymers, *Macromolecules*, 2023, **56**(5), 1995–2008.

90 Y. Matsushita, Y. Mogi, H. Mukai, J. Watanabe and I. Noda, Preparation and morphology of multiblock copolymers of the (AB)_n type, *Polymer*, 1994, **35**(2), 246–249.

91 R. M. D'Ambrosio, R. M. Michell, R. Mincheva, R. Hernández, C. Mijangos, P. Dubois and A. J. Müller, Crystallization and stereocomplexation of PLA-*mb*-PBS multi-block copolymers, *Polymers*, 2017, **10**(1), 8.

92 Y. He, D. Liu, J. Wang, P. Pan and W. Hu, Tammann analysis of the molecular weight selection of polymorphic crystal nucleation in symmetric racemic poly(lactic acid) blends, *Macromolecules*, 2022, **55**(9), 3661–3670.

93 X. Qiu, R. Liu, Y. Nie, Y. Liu, Z. Liang, J. Yang, Z. Zhou and T. Hao, Monte Carlo simulations of stereocomplex formation in multiblock copolymers, *Phys. Chem. Chem. Phys.*, 2019, **21**(24), 13296–13303.

94 D. Yablon, I. Chakraborty, H. Passino, K. Iyer, A. Doufas, M. Shivokhin, J. Thornton and B. Pittenger, Deep Learning to Predict Structure-Property Relationships of Polymer Blends, *ACS Symp. Ser.*, 2022, **1416**, 51–64.

